HYZERO

H_2 transport aircraft concept

For NASA / DLR Design Challenge 2021

Project Team

Sina Bahm

Lena Meinberg

Tobias Welsch

Simon Kotlarov

Malte Seibt

Johann Stürken

Academic Support and Advisors

Institute of Aerospace Systems, RWTH Aachen University

Univ.-Prof. Eike Stumpf

Tim Effing, M.Sc.

Submitted on July 18th, 2021

Team Members

Sina Bahm B.Sc.

Luft-und Raumfahrttechnik

(4. Semester)

Simon Kotlarov B.Sc.

Energietechnik

(1. Semester)

Lena Meinberg

Wirt.-Ing. Maschinenbau

(11. Semester)

Malte Seibt B.Sc.

Luft- und Raumfahrttechnik

(2. Semester)

Johann Stürken

Wirt.-Ing. Maschinenbau

(9. Semester)

Tobias Welsch B.Sc.

Luft- und Raumfahrttechnik

(1. Semester)

Institute of Aerospace Systems | Wuellnerstrasse 7, 52062 Aachen 415310

Univ.-Prof. Dr.-Ing.
Eike Stumpf

Wuellnerstrasse 7
52062 Aachen
GERMANY
Phone: +49 241 80-96801
Fax: +49 241 80-92233

stumpf@ilr.rwth-aachen.de

16.07.2021

Confirmation for submission

The hereby submitted project work has been confirmed by the Head of Institute of Aerospace Systems (ILR) and is endorsed for the submission in the NASA/DLR Design Challenge 2021. The work has been done independently from currently enrolled students from RWTH Aachen University without further assistance of our institute.

Univ.-Prof. Dr.-Ing. Eike Stumpf
Institut für Luft- und Raumfahrtsysteme
Rhein.-Westf. Techn. Hochschule Aachen
Wüllnerstr. 7 52062 Aachen
Telefon +49 (0)241 / 80-96800
Telefax +49 (0)241 / 80-92233

Univ.-Prof. Dr.-Ing. Eike Stumpf

Luft- u. Raumfahrtsysteme
der RWTH Aachen
Wüllnerstr. 7 52062 Aachen
Telefon +49 (0)241 / 80-96800
Telefax +49 (0)241 / 80-92233

Tim Effing, M.Sc. (RWTH)

Abstract

HyZero is a short/medium-haul aircraft for 150 passengers that is powered exclusively by liquid hydrogen. The concept, which is developed as part of the NASA/DLR Design Challenge 2021, includes a structural design, mission analysis, and a description of the required airport infrastructure. HyZero is compared with a reference aircraft which is powered with a blend of 30% Sustainable Aviation Fuel.

The basis of the development of HyZero is the identification of the specific requirements and a methodical comparison of different aircraft configurations for the development of HyZero. The most important design features derived from this include a hybrid drive train, a lifting body and high aspect ratio strut-braced wings. During the design process, special attention is paid to reduce drag and weight as well as optimally integrating the cryogenic fuel tank. To calculate the climate impact, the CO_2-equivalent as well as fuel consumption are calculated and an optimum between fuel consumption and climate impact is achieved. A noise-reduced flight path is developed for HyZero. The DOC of HyZero, which are determined using the CeRAS method for an average flight mission, are significantly higher for HyZero than the reference aircraft, as they are primarily dependent on the price of liquid hydrogen.

Zusammenfassung

HyZero ist ein Kurz-/Mittelstreckenflugzeug für 150 Passagiere, das ausschließlich mit Wasserstoff betrieben wird. Das Konzept, das im Rahmen des NASA/DLR Design Challenge 2021 entwickelt wurde, besitzt neben dem strukturellen Design auch eine Missionsanalyse sowie die Beschreibung der benötigten Flughafen Infrastruktur. HyZero wird zum besseren Vergleich mit einem Referenzflugzeug verglichen, dass mit 30-prozentigem Anteil Sustainable Aviation Fuel betrieben wird.

Die Identifizierung der spezifischen Anforderungen und ein methodischer Vergleich verschiedener Flugzeugkonfigurationen bilden die Grundlagen für die Entwicklung von HyZero. Zu den wichtigsten daraus abgeleiteten Konstruktionsmerkmalen gehören ein hybrider Antriebsstrang, ein Lifting Body sowie ein hochgestreckter Stützflügel. Beim Design liegt ein besonderes Augenmerk auf der Reduzierung von Widerstand und Gewicht sowie einer optimalen Integration des Treibstofftanks. Zur Berechnung der Umwelteinwirkung wird das CO_2-Äquivalent sowie der Treibstoffverbrauch berechnet und ein Optimum zwischen Treibstoffverbrauch und Umwelteinwirkung gefunden. Für HyZero wird ein lärmreduzierter Flugpfad erarbeitet. Die Betriebskosten (Direct Operating Cost) des HyZero Flugzeugs, sind signifikant höher als die des Referenzflugzeuges, da sie direkt mit dem Preis von flüssigem Wasserstoff gekoppelt sind HyZero ist sehr von den äußeren Rahmenbedingungen abhängig und daher besteht aktuell Handlungsbedarf diese zu ändern.

Keywords: Hydrogen, Climate Impact, Design Concept

Contents

TEAM MEMBERS I
CONTENTS IV
LIST OF FIGURES VI
LIST OF TABLES VII
ABBREVIATIONS VIII
SYMBOLS IX
1 INTRODUCTION 1
2 MOTIVATION & DESIGN PROCESS 1
2.1 AIRCRAFT REQUIREMENTS 1
2.2 REFERENCE AIRCRAFT 1
2.3 DESIGN CRITERIA 2
2.4 CONFIGURATION SELECTION PROCESS 2
3 HYZERO CONFIGURATION AND FEATURES 3
3.1 FUEL AND TANK 4
3.1.1 Fuel Selection 4
3.1.2 Tank Placement 4
3.1.3 Tank Design 4
3.2 FUSELAGE 5
3.2.1 Lifting Fuselage Design 6
3.2.2 Windowless Fuselage 6
3.3 WING AND EMPENNAGE 6
3.3.1 Wing 6
3.3.2 Stability and Control 8
3.4 HYDROGEN-BASED PROPULSION SYSTEM 8
3.4.1 Wing Mounted Engines 9
3.4.2 Boundary Layer Ingesting Propulsion 10
3.4.3 On-board Systems 11
3.4.4 Hydrogen Safety 12
3.5 TECHNOLOGY READINESS LEVELS OF KEY TECHNOLOGIES 13
4 TECHNICAL DATA 13
4.1 MASS ESTIMATION 13
4.2 AERODYNAMIC DATA 13
4.2.1 Drag 13
4.2.2 Lift 15
4.3 AIRCRAFT PERFORMANCE 15
5 AIRPORT AND HYDROGEN INFRASTRUCTURE 16
5.1 POWER GENERATION 17
5.2 HYDROGEN PRODUCTION 17
5.3 HYDROGEN LIQUIFICATION 19
5.4 HYDROGEN DELIVERY TO THE AIRPORT 19
5.5 FUELLING AND GATE OPERATIONS 20
5.6 PERMANENT INFRASTRUCTURE AT THE AIRPORT 21
5.7 TOTAL COST OF HYDROGEN PROCUREMENT AND EFFICIENCY ASSESSMENT 21
6 OPERATIONAL ASPECTS 21
6.1 FLIGHT PATH OPTIMISATION 21
6.1.1 Climate Impact from GHGs 22
6.1.2 Noise 22
6.2 OVERALL ENERGY ANALYSIS 22
6.3 DOC ANALYSIS 24
6.4 LIFECYCLE ASPECTS 24
7 CONCLUSION 25

8 REFERENCES 26
9 APPENDIX 34

List of Figures

FIGURE 2-1: LIFT COEFFICIENT VS. ANGLE OF ATTACK 2
FIGURE 2-2: MORPHOLOGICAL BOX CONFIGURATION. 2
FIGURE 2-3: OVERVIEW OF SYSTEMS AND KEY TECHNOLOGIES 3
FIGURE 3-1: GENERAL ARRANGEMENT. 3
FIGURE 3-2: TANK INTEGRATION AND STRUCTURE. 5
FIGURE 3-3: CABIN LAYOUT. 6
FIGURE 3-4: WING-FUSELAGE INTEGRATION. 7
FIGURE 3-5: HINGE OF THE FOLDING WINGTIPS 7
FIGURE 3-6: SCHEMATIC OF FISHBONE ACTIVE CHAMBER. 7
FIGURE 3-7: STRUCTURAL INTEGRATION OF THE V-TAIL 8
FIGURE 3-8: OVERVIEW OF THE DRIVE TRAIN AND MAJOR ON-BOARD SYSTEMS 8
FIGURE 3-9: ENGINE-WING INTEGRATION. 9
FIGURE 3-10: EXTRAPOLATION OF CRUISE TSFC AND OPR OVER TIME 9
FIGURE 3-11: FUEL PREHEATING IN UNDER-WING ENGINES. BACKGROUND IMAGE FROM GASTURB 13 [66]. . 10
FIGURE 3-12: BLI PROPULSOR MOUNTED ON THE AFT FUSELAGE. 10
FIGURE 3-13: ENERGY FLOW DIAGRAM OF THE CONVERSION PROCESS FROM LH_2 TO THRUST IN CRUISE. 11
FIGURE 4-1: COMPARISON OF ZERO-LIFT DRAG COEFFICIENT. 14
FIGURE 4-2: ZERO-LIFT DRAG DIFFERENCE OF HYZERO COMPARED TO THE REFERENCE AIRCRAFT 14
FIGURE 4-3: GLIDE RATIO 14
FIGURE 4-4: DRAG POLARS. 15
FIGURE 4-5: DRAG COEFFICIENT VS. ANGLE OF ATTACK. 15
FIGURE 4-6: LIFT COEFFICIENT VS. ANGLE OF ATTACK. 15
FIGURE 4-7: PAYLOAD-RANGE DIAGRAM 15
FIGURE 4-8: V-N DIAGRAM. 15
FIGURE 5-1: POTENTIAL AND SELECTED LIQUID HYDROGEN PROCUREMENT CHAIN 16
FIGURE 5-2: RAMP LAYOUT ACCORDING TO [138]. 20
FIGURE 6-1: CO_2-EQ OF BOTH REFERENCE MISSIONS. 23
FIGURE 6-2: DOC COMPARISON. 24
FIGURE 9-1: LANDING GEAR POSITION 34
FIGURE 9-2: NET PRESENT COST CALCULATIONS OF AEL AND PEMEL PLANTS 37
FIGURE 9-3: OPENVSP HYZERO 38
FIGURE 9-4: OPENVSP REFERENCE AIRCRAFT 38
FIGURE 9-5: SPECIFIC COST CALCULATION OF HYDROGEN STORAGE INFRASTRUCTURE AT THE AIRPORT. 38
FIGURE 9-6: DOC STRUCTURE 39

List of Tables

TABLE 2-1: AIRCRAFT TLARS. 1
TABLE 2-2: REFERENCE AIRCRAFT 1
TABLE 2-3: CRITERIA WEIGHTING. 2
TABLE 2-4: EVALUATION RESULTS. 2
TABLE 3-1: HYZERO DATA. 3
TABLE 3-2: CHARACTERISTICS OF PHYSICAL STORAGE METHODS [11]–[13]. 4
TABLE 3-3: GEOMETRIC PARAMETERS OF THE V-TAIL. 8
TABLE 3-4: DATA OF THE MAIN ENGINES. 9
TABLE 3-5: DATA OF THE BLI PROPULSOR. 11
TABLE 3-6: RELATED RISKS AND MEANS OF PREVENTION ACCORDING TO [83]. 12
TABLE 3-7: TRL OF KEY TECHNOLOGIES. 13
TABLE 4-1: MASS ESTIMATION. 13
TABLE 4-2: TAKE-OFF AND LANDING PERFORMANCE 16
TABLE 5-1: NET PRESENT COST IN 2035, ANNUALIZED COST & PRODUCTION COST PER KG OF HYDROGEN. 18
TABLE 5-2: SUMMARY OF SPECIFIC COST COMPONENTS OF HYZERO'S HYDROGEN. 21
TABLE 6-1: TOTAL CRITICAL MISSION ENERGY CONSUMPTION. 23
TABLE 6-2: OVERVIEW OF FUEL MASSES. 23
TABLE 9-1: SUMMARY OF MAJOR HAZARDS (LIQUID HYDROGEN SYSTEMS) ACCORDING TO [81] 36
TABLE 9-2: SUMMARY OF MAJOR HAZARDS (GASEOUS HYDROGEN SYSTEMS) ACCORDING TO [81] 36

Abbreviations

AEL	Alkaline Electrolysis
AR	Aspect Ratio
BLI	Boundary Layer Ingestion
BPR	Bypass Ratio
BWB	Blended Wing Body
CapEx	Capital Expenditure
CDA	Continuous Descent Approach
CFD	Computational Fluid Dynamics
CFRP	Carbon-Fibre-Reinforced Polymers
CG	Centre of Gravity
CIP	Consumer Price Index
CO_2	Carbon Dioxide
CO_2-eq	CO_2-Equivalent
COPV	Composite Overwrapped Pressure Vessel
CROR	Contra Rotation Open Rotor
DEP	Distributed Electric Propulsion
DLR	Deutsches Zentrum für Luft- und Raumfahrt
DOC	Direct Operating Cost
DP	Distributed Propulsion
EEG	German Renewable Energy Sources Act (‘Erneuerbare-Energien-Gesetz’)
EIS	Entry Into Service
EMC	Elastomeric Matrix Composite
EPNdB	Effective Perceived Noise Decibel
EU	European Union
EUR	Euro
FL	Flight Level
GHG	Greenhouse Gas
GWP	Global Warming Potential
HTEL	High-Temperature Electrolysis
HTP	Horizontal Tail Plane
H_2	Hydrogen
ICAO	International Civil Aviation Organization
KWKG	Combined-Heat-and-Power Levy (‘Kraft-Wärme-Kopplungsgesetz’)
MAC	Mean Aerodynamic Chord
MLI	Multi-Layer Insulation
MoNA	Modern Noise Abatement
MTOM	Maximum Take-Off Mass
NASA	National Aeronautics and Space Administration
NLF	Natural Laminar Flow
NPC	Net Present Cost
NO_x	Nitrogen Oxides
OpEx	Operating Expenditure
OPR	Overall Pressure Ratio
PAX	Passengers
PEM	Polymer Electrolyte Membrane
PEMEL	Polymer Electrolyte Membrane Electrolysis
RF	Radiative Forcing
SAF	Sustainable Aviation Fuel
StromNEV	Electricity Grid Charges Ordinance (‘Stromnetzentgeltverordnung’)
TCO	Total Cost of Ownership
TET	Turbine Entry Temperature
TLAR	Top Level Aircraft Requirement
TOFL	Take-Off Field Length
TRL	Technology Readiness Level
TSFC	Thrust Specific Fuel Consumption
USD	US Dollar
VTP	Vertical Tail Plane
ZTL	Turbofan Engine (‘Zweistrom-Turbinen-Luftstrahltriebwerk’)

Symbols

$C_{annualised}$	Annualised Cost	[EUR]
C_D	Drag Coefficient	[–]
C_{Di}	Induced Drag Coefficient	[–]
C_{driver}	Cost of Driver	[EUR]
$C_{D,0}$	Zero-Lift Drag Coefficient	[–]
$C_{el,green}$	Cost of Electricity from Renewable Sources	[EUR/kWh]
CF	Capacity Factor	[–]
C_L	Lift Coefficient	[–]
C_{NPC}	Net Present Cost	[EUR]
CRF	Capital Recovery Factor	[–]
$C_{spec,I\&O}$	Specific Cost of Investment and Operations	[EUR/kg$_{H2}$]
$C_{spec,liq}$	Specific Cost of Liquification	[EUR/kg$_{H2}$]
$C_{spec,TCO,H2-truck}$	Specific TCO of Hydrogen-Powered Truck	[EUR/km]
$c_{spec,trans}$	Specific Cost of Hydrogen Transportation	[EUR/kg$_{H2}$]
D	Landing Gear Parameter	[–]
$d_{avg,both\ ways}$	Average H_2 Transport Distance, incl. Return Trip	[km]
d_{cabin}	Cabin Diameter	[m]
d_{fslg}	Fuselage Diameter	[m]
e	Oswald Factor	[–]
$e_{spec,liq}$	Specific Energy Demand of Liquification	[kWh/kg$_{H2}$]
H	Distance Between Fuselage and Ground	[m]
i	Real discount rate	[–]
LHV	Lower Heating Value	[kWh/kg$_{H2}$]
$m_{H2,annual}$	Mass of Annual Production of H_2	[kg$_{H2}$]
N	Lifetime	[a]
n	Load Factor	[–]
P_{el}	Electric Power	[kW]
S	Area	[m^2]
v	Speed	[m/s]
V_A	Design Manoeuvre Speed	[m/s]
V_C	Design Cruise Speed	[m/s]
V_D	Design Dive Speed	[m/s]
V_{s1}	Design Stall Speed (n = 1)	[m/s]
$V_{S1,extended\ flaps}$	Design Stall Speed (n = 1) with Extended Flaps	[m/s]
W	Weight	[N]
X	Parameter Landing Gear	[–]
x_{AFTCG}	Distance Aircraft Nose aft CG	[m]
x_{Fm}	Distance Aircraft Nose Main Landing Gear	[m]
α	Angle of Attack	[°]
ρ	Density	[kg/m^3]
Δz_{CG}	Z Distance CG	[m]

1 Introduction

In 2019, the European Union (EU) presented the European Green Deal, which sets the goal of achieving climate-neutrality by 2050. Aviation is currently responsible for 3 % of global CO_2 emissions and the aviation industry has intensified its efforts to develop and implement climate-neutral flying [1]. Innovative and sustainable approaches will be needed to meet the enormous economic and ecological challenges in the coming years. To achieve the goals of the Green Deal, the use of hydrogen as a primary energy source in aviation holds great potential [2]. However, there is currently no aircraft ready for series production that runs entirely on hydrogen. The HyZero concept was developed in the context of the NASA/DLR Aeronautical Design Challenge 2021, which recognizes the need for innovation in clean aviation by calling for the design of a hydrogen-powered, short- to medium-haul aircraft with a maximum passenger capacity of 150 Passengers (PAX) and an entry into service (EIS) in 2035. The design is to be compared against a kerosene-fuelled reference aircraft with 30 % Sustainable Aviation Fuel (SAF) added at a 2035 technology level. Besides being economic and ecological to operate, in order to generate support from airlines and governments, HyZero also aims to be 'low-friction' for airport operators by requiring minimal changes to infrastructure and operations. Based on a methodical idea generation and selection process, an aircraft concept is developed that is tailored to future, environmentally friendly air transport (Chapter 2). The development of the concept, including the tank (Section 3.1), fuselage (Section 3.2), and wing and empennage (Section 3.3), is followed by the design of the propulsion system (Section 3.4). Calculations and design decisions are based on recent results from literature, as well as empirical equations. In Chapter 4, technical data like component masses and aerodynamic parameters are calculated. The description of the hydrogen procurement chain and required airport infrastructure (Chapter 5) is followed by the analysis of the operational aspects (Chapter 6). Finally, a conclusion is presented.

2 Motivation & Design Process

This chapter lists the requirements for the aircraft and its certification. In addition, the definition of the reference aircraft is discussed, and the design process of HyZero is presented.

2.1 Aircraft Requirements

Table 2-1 shows the specified numerical aircraft requirements met by HyZero. In addition, the aircraft's atmospheric effects and total energy demand are considered. HyZero targets a certification according to CS-25 [3]. Deviations are discussed in the corresponding subchapters. A flight mission analysis is conducted for reference missions of 600 and 2,000 km. The longer flight is optimized for both low climate impact and profitable operations, whereas the short one is solely optimized for minimal climate impact.

Table 2-1: Aircraft TLARs.

Reference Aircraft	Value
Passenger Number	150 PAX
Passenger Mass	80 kg and 25 kg luggage
TOFL	≤ 2000 m
Crew	80 kg (cockpit & cabin)
Cruise Speed	Ma = 0.7
Approach Speed	≤ 130 kts
Range	≥2,000 km
Diversion Range	200 NM
Flight Level	≥ 3000 m
Entry into Service (EIS)	2035
Fuel	LH_2/H_2

2.2 Reference Aircraft

The reference aircraft is developed based on the 150-PAX CeRAS CSR-01 dataset which is commonly used in conceptual aircraft studies. [4] To develop a 2035 reference aircraft in line with HyZero's targeted market entry, the CSR-01 is fitted with the CFM International LEAP-1A35A engines of the Airbus A319neo, with their performance extrapolated to 2035. In addition, a carbon-fibre-reinforced polymer (CFRP) fuselage is added. The reference aircraft is fuelled by kerosene with 30 % SAF added.The reference aircraft is not simply calculated based on HyZero's exact mission profile. Instead, educated decisions are made to achieve a meaningful comparison between the two aircraft. This includes operating the reference aircraft reference aircraft at FL 350, the flight level on which the CeRAS CSR-01 dataset is based, as to not artificially decrease its performance relative to its design point. At the same time, it only carries fuel for a 2,000 km mission to avoid a significant weight penalty. This is

Table 2-2: Reference aircraft

Reference Aircraft	Value	Unit
Take-off Field Length Dry	1,641.9	[m]
Reference Speed	130	[kt]
Climb Rate	1100	[ft/min]
Cruise Speed	0.78	[Ma]
Cruise Altitude	290	[FL]
Glide Ratio	13.02	[-]

summarised in Table 2-2. Both HyZero and the reference aircraft use a common iterative design process, which runs until the MTOM does not change more than 0.1 % after the final iteration [5].

Lift and drag of the reference aircraft for different angles of attack can be observed in Figure 2-1.

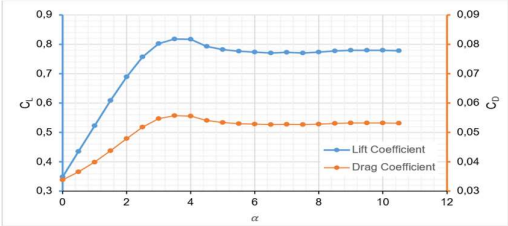

Figure 2-1: Lift coefficient vs. angle of attack

2.3 Design Criteria

To develop the most promising concept, 13 criteria are defined based on the requirements from Section 2.2. In style of [6], [7], the criteria are compared in pairs to obtain each criterion weighting. The criterion that is more important receives two points, the less important criterion zero points. If there is a tie, both receive one point each. The total number of points is added up ('Total') and its percentage of the total number of points is determined ('Weighting'), as shown in Table 2-2. The integration of the hydrogen drivetrain, the noise emissions, and the acceptance by passengers are seen as particularly important.

Table 2-3: Criteria weighting.

Criteria	Total	Weighting [%]
Passenger Comfort	2	1.28
Passenger Acceptance	10	6.41
Flight Performance	11	7.05
Stability and Controllability	12	7.69
Aerodynamics (Buoyancy)	12	7.69
Aerodynamics (Resistance)	13	8.33
Structure and Weight	12	7.69
Propulsion	19	12.18
Integration of Hydrogen Tanks	21	13.46
Certification	14	8.97
Range	4	2.56
Airport Clearance	14	8.97
Noise	12	7.69

2.4 Configuration Selection Process

According to the principle of the morphological box [7], [8], the aircraft is divided into nine largely independent main categories such as layout, propulsion, and tank shape. Options for each category are identified through an extensive literature investigation. The results are shown in Figure 2-2. The options can be freely combined between the main categories, resulting in several concept proposals.

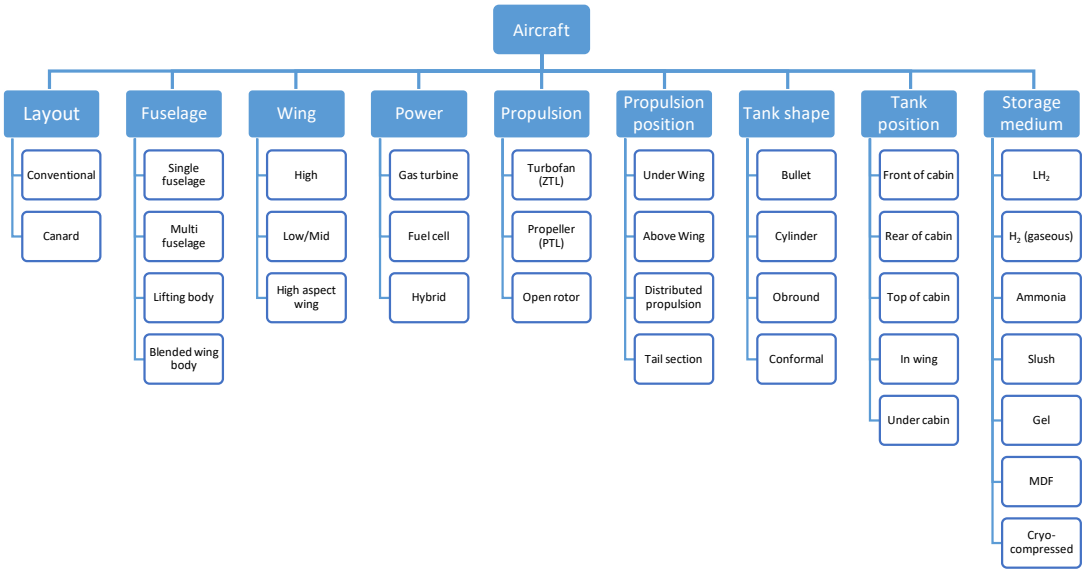

Figure 2-2: Morphological box configuration.

Table 2-4: Evaluation results.

No.	Configuration	Average Score	TCR [%]
1	Canard, single fuselage, low wing, gas turbine (turbofan, above wing), LH_2 tank (conformal, in wing)	3.1	62
2	Multifuselage, mid wing, gas turbine (turbofan, under wing), LH_2 tank (cylinder, rear of cabin)	3.0	60
3	Single fuselage, mid wing, hybrid (open rotor, tail section), LH_2 tank (cylinder, front of cabin)	3.3	66
4	Blended wing body, hybrid (turbofan, tail section), LH_2 tank (conformal, in wing)	2.7	54
5	Lifting body, high aspect ratio wing, hybrid (turbofan, under wing), LH_2 tank (rear of cabin)	3.9	78

Based on an initial assessment, five of these concepts are deemed feasible and technologically diverse enough for further investigation. The concepts are evaluated by means of a utility analysis according to HERBIG [6], based on the degree of fulfilment from excellent (5 points) to unusable (1 point) for each criterion. The results of the evaluation, as well as the technical compliance rate (TCR), which expresses the conformity of each configuration with the requirements, are shown in Table 2-4. The fifth concept achieves the highest average score and a technical compliance rate of 78 % and is therefore selected as the basis of the following design process of HyZero. Figure 2-3 visualises all systems and key technologies of the concept, which is discussed in more detail in the following chapter.

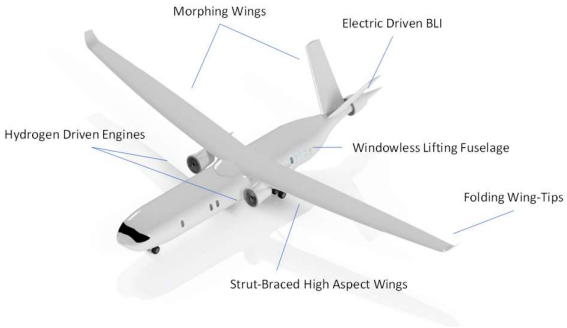

Figure 2-3: Overview of systems and key technologies.

3 HyZero Configuration and Features

HyZero is a fixed-wing aircraft with a V-tail. The high wing has a high aspect ratio and is supported by struts. The tank, which contains two independent compartments separated by a dividing wall, is located in the rear of the aircraft. Instead of an elliptical shape, the fuselage cross-section features a double-D profile. The two main engines are mounted under the wing. In addition, a boundary layer ingesting (BLI) fan, powered by a fuel cell, is integrated at the rear of the fuselage, as shown in Figure 3-1. The main aircraft dimensions and characteristics are gathered in Table 3-1.

Table 3-1: HyZero data.

Aircraft	
Length	35.82 m
Height	8.06 m
MTOM	59,063 kg
Wing Area	119 m^2
Aspect Ratio	19.55
Anhedral	3°
Sweep Leading Edge	9.16°
Taper Ratio	0.5
Empennage Area	36.37 m^2
Take-off Field Length Dry	1,553.5 m
Landing Field Length	980.3 m
Climb Rate	1,700 ft/min
Cruise Speed	Ma 0.7
Cruise Altitude	FL 290
Glide Ratio	18.86

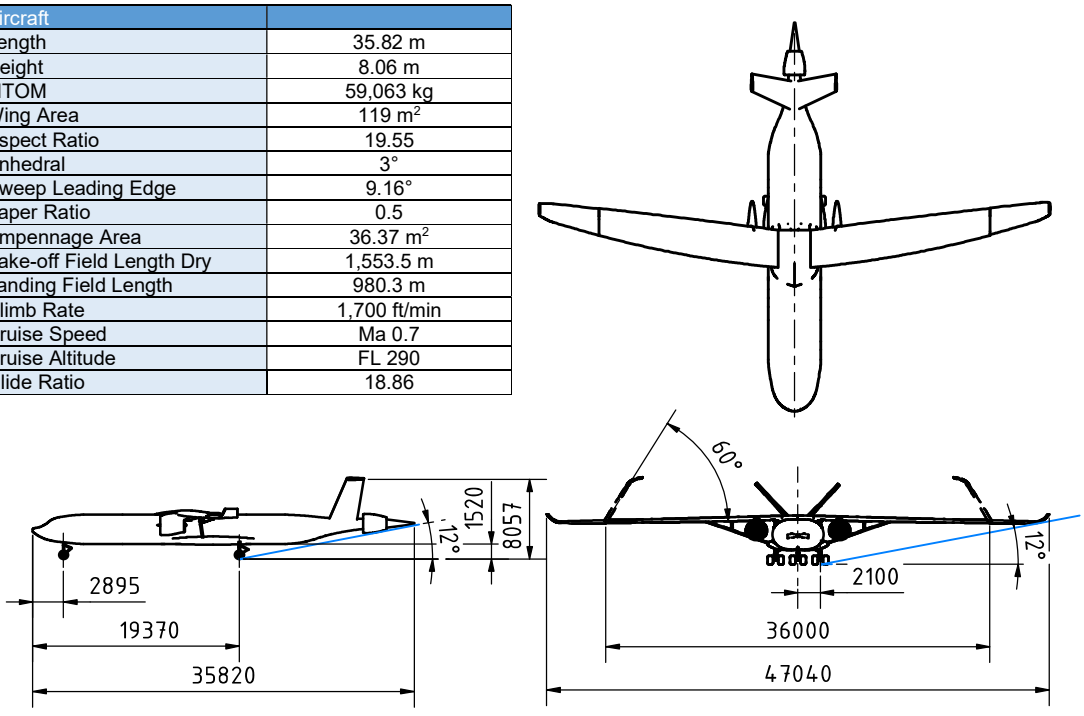

Figure 3-1: General arrangement.

Figure 3-1 also features the geometric proof for the clearance angles. Both the tail clearance and the wing clearance angle are approximately 12°. A detailed calculation of the clearance angles and the associated configuration of the landing gear is given in Appendix A. The calculation of the remaining values from Figure 3-1 , as well as the design process as a whole, are discussed in the following sections.

3.1 Fuel and Tank

Integration of tanks and fuel system is a major design factor for hydrogen-powered aircraft. In this chapter, the fuel selection and tank design processes are detailed.

3.1.1 Fuel Selection

One possible classification of hydrogen storage technologies is the segmentation into physical storage, adsorption, and chemical storage methods [9]. Adsorption and chemical storage methods are largely differentiated by the carrier material. Because of the necessity of using these carrier materials, all adsorption and chemical storage methods suffer from either low volumetric or gravimetric energy densities, and are deemed unsuitable for aircraft applications in 2035 based on energy density assessments [9], [10]. Physical storage includes compressed, liquified, and cryo-compressed hydrogen. Table 3-2 summarises key characteristics of these methods according to RIVARD ET AL., BRUNNER ET AL., and THANH ET AL. [11]–[13]. The data allows for a rough comparison, although values, especially the gravimetric system capacity, or weight of hydrogen per total tank system mass, vary between tank sizes and applications [11].

Table 3-2: Characteristics of physical storage methods [11]–[13].

	Storage pressure [bar(g)]	Storage temperature [K]	Density [kg/m³]	Volumetric energy density [kWh/m³]	Gravimetric system capacity [wt%]
compressed	700	293	26.3	885	5.2
compressed	350	293	17.6	590	5.5
cryo-compressed	300	40 – 80	80 – 60	2,690 – 2,020	5.4
liquid	0	20	70	2,350	7.5

In addition to safety, mass and volume are the two most important characteristics of a hydrogen tank system for aircraft applications. Liquid hydrogen has by far the highest gravimetric system capacity, meaning it requires the least amount of tank mass to store hydrogen. This stems from the high mass of the pressure vessels required for compressed and cryo-compressed storage. In addition, pressure vessels are costly and limited to near spherical or cylindrical shapes. [11] The slight advantage of cryo-compressed storage, which combines cryogenic and pressure storage, in terms of volumetric energy density does not offset these significant drawbacks. Under consideration of other factors such as transportability, handling, and energy requirement for compression and liquification, respectively, liquid hydrogen is selected as the fuel for HyZero.

3.1.2 Tank Placement

To minimise heat influx and boil-off, the surface of the LH_2 tanks must be minimized, leading to compact, near-spherical or cylindrical shapes. The amount of LH_2 required for HyZero makes tank integration into its wings impossible. As the tanks must be placed outside of the pressurised cabin for safety reasons [14], and cargo space cannot be cannibalised, the only options seen as reasonable are in front or behind the cabin, or under the wing as removable tanks. Because of the decision to place the BLI propulsor at HyZero's aft section, placing the tanks in the front section of the fuselage is dismissed due to the prohibitively long fuel lines this would require. Removable tanks under the wing offer the benefit of allowing not only the reduction of fuel mass, but also fuel tank mass for the shorter, 600 km mission. They also have the potential to significantly simplify and accelerate the refuelling process. External tanks are widely used by military fighter aircraft and have been proposed by Airbus for their future hydrogen aircraft, albeit as standalone propulsion units [15]. The additional drag from external pods for an Airbus A321 was evaluated by DANGI AND PATEL [16]. Even for the most favourable option, total drag force still increased by 26.51 %. [16] In the same study, an increase in length of the aircraft to accommodate the hydrogen tanks increase drag by only 6.85 % [16]. For this reason, the option of carrying HyZero's hydrogen in removable, external pods is not pursued further. This leaves the area behind the cabin as the only feasible option. Placing removable tanks within the aircraft offers the benefit of significant mass reduction for the shorter mission without disadvantages in drag induced by external pods. However, the installation of large doors for tank loading would disrupt the boundary layer, significantly reducing the efficiency of the BLI fan. Therefore, the installation of a permanent tank in the aft section of the aircraft is selected for the HyZero concept. The challenge of maintaining an allowable centre of gravity (CG) range influences the placement of heavy systems like the fuel cell. A benefit of the fuel placement within the fuselage, as opposed to the wing, lies in the fact that their aerodynamic shape can be optimized and innovative concepts such as morphing wings, which are discussed in Section 3.3.1, can be implemented.

3.1.3 Tank Design

The single tank with two compartments is designed as an integral, load-carrying part of the fuselage, as this leads to reductions in structural mass compared to the non-integral option [17]. In addition, non-integral tanks have to be removed entirely for maintenance, whereas an integral tank can often be

serviced simply by removing panels [18]. The tank is insulated externally rather than internally. This means that the cryogenic hydrogen is in contact with the tank wall. To avoid excessive strain from thermal cycling, the tank should be kept in a cold state, unless inspected for maintenance [19]. Despite this operational disadvantage of external insulation, internal insulation is not an alternative, as there is currently no material available, or likely to be available until 2035, that can sufficiently prevent permeation through the insulation [20].

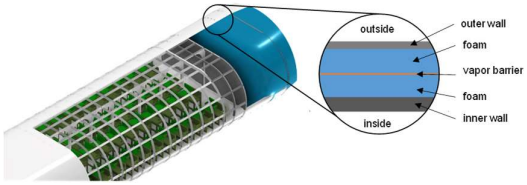

Figure 3-2: Tank integration and structure.

Composite tank walls can provide a 25 % weight saving over aluminium tanks [21]. Despite their higher cost, a composite tank design is adopted to keep the CG within an acceptable range. A liner made of aluminium is necessary to prevent the hydrogen from leaking through the composite material [18]. VERSTRAETE ET AL. explore multi-layer insulation (MLI) and foam insulation for applications comparable to those of HyZero. While MLI does provide a weight advantage over foam for the same level of heat flux, its use of a high vacuum makes it more expensive to install and maintain, and carries the risk of catastrophic failure in case the vacuum is lost. [22] In addition, the use of foam insulation only requires a single structural tank wall rather than two. The outer tank wall only serves as a barrier between the foam and the environment. [18] A polyurethane foam is selected as it achieves the lowest mass [22]. The tank is integrated into the fuselage according to the description by BREWER [18]. The tank features a diving wall that produces two separate compartments, creating redundancy and ensuring that the main engines can be fed from separate engines during take-off [23]. In addition, the tank is equipped with additional dividers to cut down on sloshing [18]. The final tank design and integration into the structure are shown in Figure 3-2. The tank wall is calculated using the pressure vessel equation, which considers the tensile strength of the tank wall material, a safety factor, and the pressure difference between the inside and outside of the tank (Appendix L) [24]. In addition, the wall thickness depends on the diameter, so different wall thicknesses are necessary for the HyZero tank shape. It is assumed that the outer tank wall has a constant thickness, which is calculated for the most stressed point. The separating wall in the middle is calculated equally using twice the total length as diameter to maintain redundancy in case one compartment leaks. The overall tank mass can be seen in

Table 4-1: Mass estimation.

Component	Mass [kg]			Mass [kg]	
	HyZero	Ref. Aircraft	Component	HyZero	Ref. Aircraft
Fuselage	9117 [92]	9072 [92]	Design Payload	15750	15750
Wing	9516 [50]	7200 [24]	Block Fuel	1562	6277
Empennage	539 [47]	896 [1]	Σ MTOM	56132	60864
Landing Gear	1736 [93]	2633 [93]			
Propulsion	8801	7913	Pylon	979 [24]	979 [24]
Tanks	1090		Hydrogen Pipes	20	
Flight Systems	4145 [92]	4247 [92]	Main Engines	3320 [24]	3330 [24]
Σ MME	34944	31961	BLI+ Systems	870	
Operating Items	2225 [92]	2225 [92]	Nacelle	2023 [24]	2012 [24]
Furnishings	4651 [93]	4651 [93]	Engine Systems	1589 [24]	1592 [24]
Σ OME	41820	38837	Σ Propulsion	8801	7913

Table 4-1 calculated as shown in Appendix L.

3.2 Fuselage

This chapter details two key aspects of HyZero's fuselage design: its lift-generating characteristics, as well as the windowless design. The decision-making process and the implementation are explained.

3.2.1 Lifting Fuselage Design

HyZero's fuselage is a lifting body. The cross-section consists of two D-shaped sections joined in the middle, following the model of the Aurora D8 concept. This fuselage cross-section design is the lightest among several investigated by MUKHOPADHYAY ET AL. [25] While not currently in operation, the technology is anticipated to be ready for commercial applications in 2035 [26].

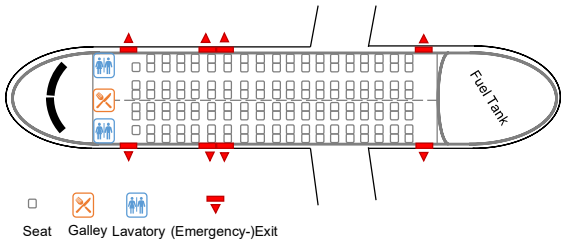

Figure 3-3: Cabin layout.

Due to the non-circular shape of the cabin, the internal cabin pressure leads to considerable bending stresses at the transition of the circumference from half-cylinders to the straight top and bottom sections. As opposed to a tubular fuselage, the wall structure must be stressed. The increased fatigue and circumferential stresses can be balanced via the vertical inter-cabin wall. Based on the PRSEUS model [27], the fuselage is made of carbon fibre preforms [25], [28]. Despite these complications, the lifting body design offers significant advantages over conventional construction. Since the tank is the most important design driver in HyZero's design, the fuselage is optimised around the tank. Based on the tank dimensions, as well as standard values for seats, aisles, etc., the dimensions of the fuselage are determined. Also included in the calculation is a cargo compartment below the passenger cabin. The 4.48 m width and 2.98 m height of the fuselage allows a 2-4-2 twin aisle seating that is unusual in the short-haul aircraft class. The lavatories, galleys, and emergency exits are considered (cf. Figure 3-3). The overall fuselage length can be reduced to 35.82 m, resulting in a more favourable fuselage pitching moment. The wetted area is increased compared to an aircraft with the same capacity and a round cross-section of the same height, as the increased wetted area due to the larger cross-section circumference outweighs the reduction from the shortened fuselage (cf. Section 4.2.1). Nevertheless, HyZero's fuselage design offers aerodynamic advantages. On the one hand, the fuselage contributes to lift due to its wide design. [29] On the other hand, it increases aerodynamic efficiency due to its bell-shaped lift distribution. This allows for the narrower and lighter design of the wings, leading to fuel savings [30]. Another advantage is the guidance of the air along the fuselage, allowing the use of a BLI fan at the aft section, which is discussed in Section 4.2.1. The geometric design of the tail-section is based on a study by HABERMANN [31]. Despite its streamlined design, the tail section offers sufficient space for the tank.

3.2.2 Windowless Fuselage

In the style of the Emirates First Class of the Boeing 777-300ER, the design of HyZero largely eliminates windows [32]. Instead, there are 77" OLED screens showing a virtual representation of the outside world, augmented by infotainment content connected to small external cameras. [33], [34] The screens are clad in the traditional oval window design, promoting passenger acceptance. Since for safety reasons, under part 25 of the CS-25 Regulations Amendment 12, aircraft 'shall have means to view conditions outside the exit with the exit closed', the doors and emergency exits continue to have windows [3].

Eliminating windows from the uninterrupted fuselage allows for fuselage weight savings of up to 25 %, depending on fuselage size, which in turn leads to a reduction in fuel costs despite increased energy consumption by screens and cameras. In addition, the design leads to a reduction in manufacturing costs and an increase in resistance to fatigue damage. [33], [34]

3.3 Wing and Empennage

HyZero is equipped with a high wing with a high aspect ratio, and a V-tail. The wing is supported by jury struts. This chapter elaborates on these components.

3.3.1 Wing

HyZero's high-wing configuration, combined with the wing sweep of 8.2°, contributes to a negative sideslip-induced roll moment. To limit this moment and increase stability, an anhedral of 3° is chosen for the wing. Additional features of the wing are detailed below.

High Aspect Ratio

In conventional aircraft, induced drag is responsible for roughly 35 % of overall drag [35]. For a finite wing with an elliptical lift distribution, the induced drag coefficient is inversely proportional to the aspect ratio [36]. Because of this, HyZero features a high aspect ratio wing. Conventional short-range aircraft, such as the reference aircraft, have wing aspect ratios of 9 to 10. Modelled on the concept of [37], the aspect ratio for HyZero is raised to 19.55. The lift induced drag coefficient can be written as $C_{D_i} = \frac{{C_L}^2}{\pi * e * AR}$, with $AR = \frac{b^2}{S}$ [38]. The selected aspect ratio therefore results in a lift-induced drag reduction of 51.5 %, which leads to an overall drag reduction of about 18 % for a constant Oswald factor $e = 0.85$. The aspect ratio is limited for structural and airport logistics reasons. A large wingspan causes problems in ground handling. As the wing generates lift during flight, a higher wingspan has the disadvantage of a longer lever arm that exerts a higher bending moment onto the root of the wing. In addition to structural problems in the wing box area, the thin wing can induce flutter motions during flight [39]. Figure 3-4 shows an illustration of HyZero's wing-fuselage integration. The following sections address how HyZero solves the described challenges.

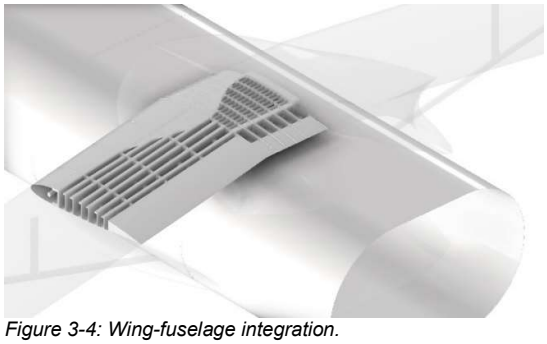

Figure 3-4: Wing-fuselage integration.

Strut-Braced Wing

NASA [37] investigates the optimal aspect ratio and the number of additional vertical supporting jury struts in relation to minimal fuel consumption and wing mass. Namely, they analyse whether the wing mass reduction enabled by adding struts and jury struts is worth the increase in drag. A single strut with one jury strut is found to be optimal, which is visible in Figure 3-1 [37]. For the lowest possible structural weight of the strut, a one-dimensional tensile load distribution along the bar axis is required. However, due to the unavoidable aerodynamic interference, as well as the vertically impinging jury, a multidimensional load is considered in the design .

Folding Wingtips

To achieve a maximum wingspan of less than 36 m when operating on the ground, HyZero's wingtips can be folded up after landing. The hinge mechanism enabling this is shown in Figure 3-5 The system and additional structural wing mass increase the wing mass by 10 % [40]. Its wing-folding capability allows HyZero to be categorised as a Code C aircraft according to ICAO Annex 14 [41]. This gives HyZero operators the advantage of only needing to pay Code C fees at the airports [37]. In addition, take-off and landing is possible at many regional airports, which is particularly important for short-range flights. For HyZero, it is essential that the wings are in the unfolded state in flight and during take-off and landing. This certification challenge has already been solved by Boeing with their 777X, which means that the certification guidelines are established [42].

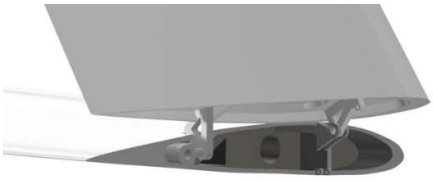

Figure 3-5: Hinge of the folding wingtips.

Morphing Wing Flap System

Since no fuel is stored in HyZero's wing, there is ample room for improvement of wing aerodynamics, including the installation of a morphing camber system. Traditional aircraft design aims to optimize aerodynamics and other factors with regard to a specific design point. As a result, every point other than the design point is suboptimal. During an aircraft's mission, however, many different conditions are encountered. With its morphing wing technology, HyZero can adapt to these different flight conditions.

The camber in an airfoil has significant impact on the generated forces. Camber variation is used to generate high lift coefficients [44]. In current aircraft, this is realized with the help of flaps, especially along the trailing edge. While highly effective for camber variation and area enlargement, flaps have several disadvantages that cannot be eliminated without rethinking the whole system. An abrupt change in camber results in an increase of drag over the baseline airfoil and can lead to an early flow separation at the trailing edge, which

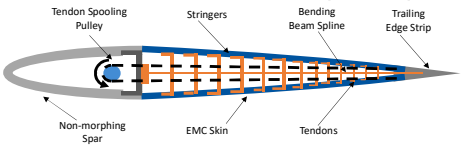

Figure 3-6: Schematic of fishbone active chamber.

again limits the maximum lift coefficient [45]. As flaps are separate components, gaps in the surface are inevitable, causing drag and noise. [46] The morphing wing technology of HyZero solves these problems. The morphing concept is derived from the Fishbone Active Camber (FishBAC) concept [43], shown in Figure 3-6. It is built around a highly anisotropic, compliant structural core with a pre-tensioned elastomeric matrix composite (EMC) skin. This allows for low part numbers, which increases reliability, while combining a low chordwise stiffness with a high spanwise stiffness [43]. Wind tunnel testing confirms that the morphing system is able to increase the lift coefficient by $\Delta C_L = 0.72$ at $\alpha = 0°$, which is nearly identical to that of a 25 % chord flapped airfoil. The tests show a significant improvement in lift over drag ratio of 20-25 % [45].

3.3.2 Stability and Control

A V-tail helps to decrease induced drag and empennage mass [47]. Due to challenges regarding ground clearance, an inverted V-tail as proposed by RAYMER [44] cannot be used for HyZero. Although it does not reduce the wetted area significantly [48], the advantages result it its integration into HyZero as shown in Figure 3-7.

Table 3-3: Geometric parameters of the V-tail.

Symbol	Description	Value	Unit
SM	Static Margin	5.15	[%]
ν	Dihedral	53.36	[°]
S_V	Area	33.62	[m^2]
φ_{LE}	Leading Edge Sweep	14.16	[°]
l_μ	MAC	2.52	[m]

A two-step process is used for designing the V-tail. First, a conventional cruciform tail is sized and then the horizontal tail plane (HTP) and vertical tail plane (VTP) are combined into a single V-tail.

The HTP is sized such that lateral stability in cruise, and sufficient controllability are achieved. The static margin should be kept between 5 % and 10 % of the mean aerodynamic chord (MAC) [24]. In the case of HyZero, a static margin of 5.15 % is achieved. The aspect and taper ratios of the HTP are initially chosen from empiric intervals by ROSKAM and it is ensured that they do not exceed the boundaries throughout the iterative process [49]. For the VTP, both weathercock stability and control over the aircraft in case of an engine failure must be achieved. This is expressed by a positive yawing moment derivative due to sideslip ($C_{n\beta} > 0$). The investigation is conducted for the entire CG range from front to aft position. Depending on the specific case, either the front or aft CG position is the critical case.

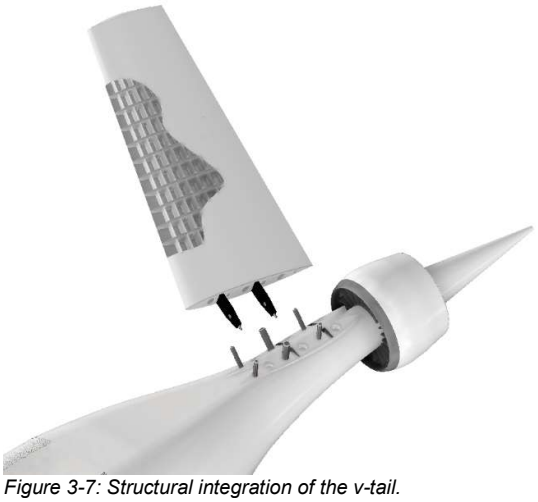

Figure 3-7: Structural integration of the v-tail.

After sizing both the HTP and VTP, (3-1) and (3-2) are used to size the V-tail. [48] While (3-1) calculates the dihedral angle of the V-tail, (3-2) combines the HTP and VTP area to give the area of the V-tail. The constant K accounts for insufficiencies of the V-tail and achieves an adequate wetted area. [48] The aspect and taper ratios of the HTP [49] are used for the V-tail, as it is more similar to the former than the VTP. The static margin and a selection of geometric parameters are given in Table 3-3; the relevant derivates can be found in Appendix B.

$$\nu = \arctan\left(\sqrt{\frac{S_{VTP}}{\mathrm{K}\cdot S_{HTP}}}\right) \tag{3-1}$$

$$S_V = \frac{S_{HTP} + S_{VTP}}{\cos^2(\nu) + \mathrm{K}\cdot\sin^2(\nu)} \tag{3-2}$$

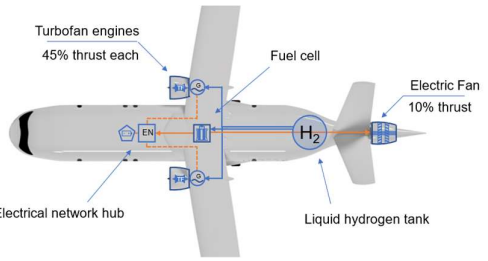

Figure 3-8: Overview of the drive train and major on-board systems.

3.4 Hydrogen-Based Propulsion System

For HyZero's propulsion system, conventional turbofan engines are chosen as the main propulsors. A pure fuel cell-electric propulsion is disregarded due to the lacking technology level of fuel cells today, and the insufficient improvement of the same anticipated until EIS in 2035. In particular, durability and reliability under aeronautic conditions is a topic not sufficiently addressed by research [51]. Figure 3-8 shows a schematic of HyZero's powertrain fitted to the design requirements. A parallel-hybrid system of novel propulsion technologies is selected. One of these, namely BLI, is identified as a key technology for lifting body concepts like

HyZero [50], cf. 3.2.1. The electric power for the aft BLI fan is provided by a fuel cell. Small generators in the turbofan engines serve as emergency power supplies and as engine starters. Battery storage is kept to a minimum to only serve peak power loads or in case of system failure. A relatively low thrust is assigned to the BLI propulsor to harness the BLI benefit, while retaining larger and more efficient engines underneath the wings. The individual parts of the propulsion system are discussed in detail in the following chapters, starting with the wing-mounted engines. After that, the BLI propulsion system and remaining on-board systems are presented.

3.4.1 Wing Mounted Engines

The overwhelming majority of civil transport aircraft use engines mounted below the wing. The ease of maintenance along with a significant wing bending relief are driving factors [52]. HyZero utilises a shoulder wing configuration, making the wing mounted engines even more attractive due to large ground clearances being available for high bypass ratio engines. Figure 3-9 shows the engine position under the wings. Being a short to medium haul aircraft with a design range of 2,000 km, only a limited time is spent in cruise. Therefore, future concepts must be evaluated carefully to ensure an overall benefit besides static cruise operation.

Figure 3-9: Engine-wing integration.

Engine Parameters

A promising optimisation of under-wing engines is the boosted turbofan concept [53], [54]. Boosted turbofans allow greater flexibility of setting engine power, independent of the current thermodynamic operating conditions of the engine. However, the variations in thrust of a high-bypass turbofan engine at constant throttle, as the altitude changes over the flight path, already align well with the mission requirements. This leaves little to be gained from the boosted turbofan concept, which would significantly increase aircraft weight [55]. Therefore, conventional gas turbines with the necessary adaptations to hydrogen fuel, are selected.

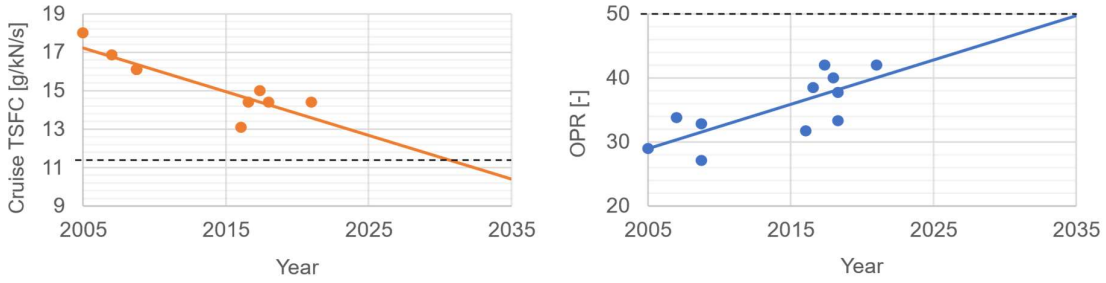

Figure 3-10: Extrapolation of cruise TSFC and OPR over time.

An important design aspect of modern engines is the bypass ratio (BPR). With an increase in BPR, the thrust-specific fuel consumption (TSFC) decreases due to a higher propulsive efficiency. At the same time, the system weight increases drastically, as does the nacelle drag [56]. For a one engine out scenario, a larger tailplane is needed due to higher windmill drag of the damaged engine [57]. A BPR of 14 is found to be optimal for future regional aircraft [56], [58]. To keep the outer diameter of the engine to a minimum, core size needs to be reduced. This commonly reduces the thermodynamic efficiency of the core, due to lower channel height in the compressor. The blades need to be redesigned to deal with the resulting large relative tip clearance and low stability margin. Also, the blade thickness cannot be simply reduced due to material and manufacturing limits along with safety margins for foreign object damage, leading to increased blade profile loss [59]. An extrapolation of engine characteristics is done based on engines with market entry between 2005 and 2020, cf. Figure 3-10. Only engines with a thrust range of 90-150 kN are included, due to the very different balance between operating and manufacturing cost of other engine sizes resulting in different designs [60].

An overall pressure ratio (OPR) of 50 is chosen for the engine cycle. The last compressor stages are replaced by a radial stage to enable even lower channel heights [61]. Based on the extrapolation, a TSFC of 11.5 g/(kN*s) is estimated for a kerosine driven engine. This

Table 3-4: Data of the main engines.

Parameter	Value
Fan diameter	2.10 m
Take-off thrust	85 kN
Cruise TSFC	4.1 g/(kN*s)
OPR	50
BPR	14

estimate is done conservatively due to uncertainty in the data. The difference in heating value alone would put the equivalent TSFC for hydrogen at 4.12 g/(kN*s). However, fuel consumption is even lower because of hydrogen's unique properties, as discussed in the following. An overview of some engine parameters is given in Table 3-4.

Hydrogen Integration

Running a conventional gas turbine with hydrogen as fuel requires some design changes, in particular for the burner injector. Generally, no carbon is present in the fuel, eliminating CO_2 as a combustion product along with soot, unburned hydrocarbons, and carbon monoxide. The fuel is clean and free of impurities to either erode or corrode the hot sections of the engine However, hydrogen embrittlement is a real challenge [18]. Water is the primary product with small amounts of nitrogen oxides (NO_x). Compared to a conventional engine, NO_x can be reduced by 75 % due to favourable material properties [1]. The main factors in NO_x generation are temperature, pressure, dwell time, and equivalence ratio [63]. Hydrogen has wide flammability limits, allowing lean combustion at lower temperatures. In addition, the very high burning velocity and the diffusivity of hydrogen minimise the dwell time of the reactants in hot areas, leading to a further decrease in NO_x [64], [65].

Improved hydrogen combustor technology, like micro-mix injection, contributes to the emission reduction as well. The technology works by introducing interfering gaseous fuel and oxidizer jets, enhancing fuel mixing greatly. A side effect of a more homogenous temperature distribution is lower thermal stress in the combustor, aided by the low emissivity of a hydrogen/air flame [18].

As previously noted, the necessary fuel mass flow is about a third of that of a comparable kerosine engine. This leads to a direct reduction in engine thrust through lower overall mass flow. The accompanying change in gas composition, however, cause a small net increase in thrust [63]. HyZero stores all necessary hydrogen at cryogenic temperatures. Prior to combustion, the fuel needs to be heated up to compressor exit temperatures to avoid severe efficiency losses. Hydrogen has a very high specific heat capacity, making it perfect for synergistic cooling applications in the engine. Starting at the front of the engine, precooling of compressor air promises to reduce the required compressor work and increase OPR. However, benefits are limited especially for smaller engines. In addition, precooling poses many challenges, like risk of ice formation and foreign object damage, to the heat exchanger and is therefore excluded [18], [67].

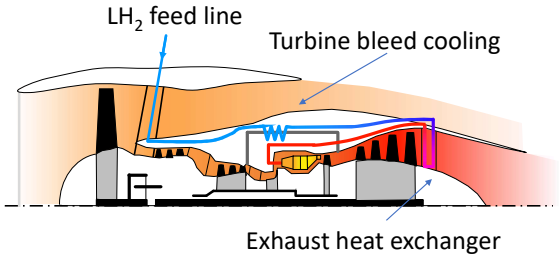

Figure 3-11: Fuel preheating in under-wing engines. Background image from GasTurb 13 [66].

As a result, a less intrusive technology, cooling the turbine bleed air, is chosen. Thus, lower cooling mass flow is needed, increasing the thermodynamic efficiency. Turbine Entry Temperature (TET) can also be increased by at least 100 K [68], leading to benefits for many aspects of the engine. The energy that can be harnessed from cooling the turbine cooling air is small. Therefore, a heat exchanger aft of the low-pressure turbine is installed to provide the energy to preheat the fuel to relevant temperatures, cf. Figure 3-11. The weight penalty is more than compensated by the reduction in fuel consumption [18].

3.4.2 Boundary Layer Ingesting Propulsion

In addition to the under wing mounted high bypass engines, 10 % of cruise thrust is supplied by a BLI propulsor. This share is set to the minimum value to harness large wake-filling benefits while limiting the weight increase of the aircraft. The BLI concept from [69] uses a slightly lower thrust share for the BLI fan, resulting from the far larger overall aircraft. Another concept from [70] implements a relatively larger BLI system for a similar aircraft size, theoretically achieving even higher benefits. This is justified by the long flight range of the aircraft, where fuel consumption has a large influence on overall operation cost [60]. Another reason for choosing a lower thrust share for the BLI fan is the utilisation of hydrogen and its extremely low gravimetric density. So, an increase in block fuel is not significantly increase overall aircraft weight.

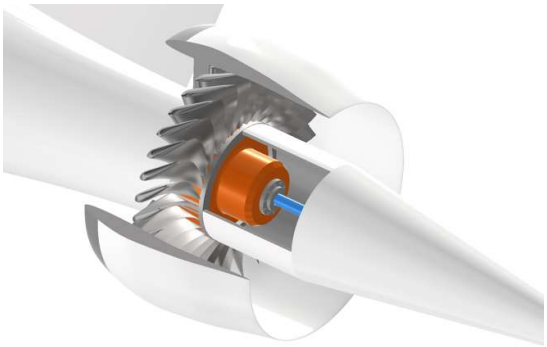

Figure 3-12: BLI propulsor mounted on the aft fuselage.

As mentioned, the benefits from ingesting the slower velocity boundary layer flow are the reduction in jet and wake losses of the aircraft resulting in lower overall thrust requirements [71]. Further benefits are a slight decrease in TSFC compared to the turbofan engines due to a more efficient, yet also heavier, drivetrain [72]. The propulsor is positioned aft on the fuselage, as most viscous drag of an aircraft arises from to the fuselage, especially for the implemented lifting body concept [71]. A full annular inflow is chosen to provide maximum benefit for a single engine configuration, since the main engines are installed under the wings [73], [71]. The BLI fan is illustrated in Figure 3-12: BLI propulsor mounted on the aft fuselage., along with key parameters in Table 3-5. Mass estimation is not included and can be found in Section 4.1. A downside to utilizing the boundary layer flow is a distorted inflow resulting in performance loss of the BLI fan [74] – [75]. However, for an axisymmetric inflow the losses are minimal compared to one-sided BLI configurations [71]. Due to the low total pressure in the hub region, the fan root needs to be redesigned to yield any useful work. Moreover, the fan blade could operate near the design point in the clean flow area and stall as it travels through a disturbance from the wings, fuselage upsweep or the empennage [76].

Inlet guide vanes would be one option to homogenise the inflow [69]. They are not implemented in the final design due to weight considerations and possible future improvements in minimising the disturbances. The outlet guide vanes are therefore an important structural component for the nacelle.

Table 3-5: Data of the BLI propulsor.

Parameter	Value
Fan diameter	1.65 m
Cruise thrust	4 kN
Propulsive efficiency	0.9
Electrical efficiency	0.95
Cooling	LH_2

The BLI fan operates at full load for most of the flight sections. The placement of the fan is not protected against foreign object damage. Therefore, the fan is shut off entirely on take-off and landing.

3.4.3 On-board Systems

Using hydrogen as an energy source for the aircraft requires changes in many systems to allow for optimal operation. This opens the possibility for new synergies to be utilised, like using the cryogenic hydrogen for cooling/coolant. This is applied for both the electric system of the BLI propulsor, decreasing ohmic losses significantly [77], as well as the fuel cell, recuperating the waste heat. The polymer electrolyte membrane (PEM) fuel cell is also responsible for a wing anti icing system. The necessary hydrogen is supplied by two separate fuel lines. From these, one extracts the boil-off from the tanks. This opens the possibility to control the temperature level inside the tank by lowering pressure levels and therefore letting more gas boil-off, cooling the tank. The usual boil-off rate is well below the fuel consumption rates, so, the second feed line carries liquid hydrogen and is shared with one of the main engines. In general, both main engines are capable of being fed from each of the two hydrogen tanks. For emergency situations, the fuel cell is not an essential system as back-up power does not need to drive the BLI propulsor. 40 kWh of battery storage and emergency power from the main engines are capable of covering the power need of essential systems. Hydrogen carrying pipes need to be insulated to minimize heat leak into the fuel as well as limit the frost build-up and subsequent water accumulation inside the fuselage [50]. Foam insulation is chosen, as vacuum jacketed lines require more maintenance and are more expensive. Low pressure fuel pumps are used in proximity to the tank with the main pumps being located at the under-wing engines [18]. Conventional control systems are used for the systems not mentioned in detail, including landing gear, flight control, and more.

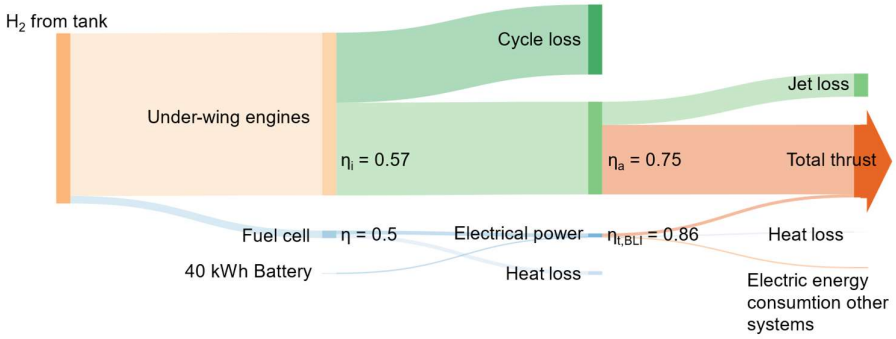

Figure 3-13: Energy flow diagram of the conversion process from LH_2 to thrust in cruise.

Operating a PEM fuel cell under aeronautical conditions is a major challenge for current technology. First, the inlet air needs to be filtered for sulphur compounds as well as carbon monoxide to extend the

service life of the fuel cell [78]. The low atmospheric pressure at cruising altitude is also detrimental to fuel cell performance, requiring a more powerful compressor [79]. Other research suggests adjusting the cathode stochiometric ratio to compensate the performance loss [51]. The chosen PEM fuel cell comes with low overall weight, the capability to be scaled to size and a relatively quick response time to load changes [80]. Thus, only a small battery storage is needed to cover high load variations. The energy conversion chain can be seen illustrated in Figure 3-13. Incoming flows are the hydrogen from the tanks along with the minimal power influx from the batteries. Outgoing energy flows are the thrust power and electrical energy for the on-board grid, as well as large waste heat fluxes. The heat recuperation with liquid hydrogen is not shown in the diagram.

3.4.4 Hydrogen Safety

This chapter deals with the safety risks and requirements during flight, associated with the use of hydrogen. It focuses on the period between take-off and landing. Hydrogen is a colourless, odourless, and non-toxic gas that is lighter than air above -23.15 K [81]. The low ignition energy of 0.017 mJ [82], the wide range of flammability, and the high volatility pose a risk of combustion [18], [81], [83]. While the fuel is not considered a hazardous substance for humans or the environment [84], there is a risk of asphyxiation due to the displacement of oxygen [81]. Although hydrogen is considered by BREWER [18] to be of similar safety criticality as conventional aviation fuels, it should be handled with care to ensure the safety of people, the environment, and the aircraft [18].

Table 3-6: Related risks and means of prevention according to [83].

Related Risks	Means of Prevention/Protection
Volume expansion of LH_2 Trapped liquid	• Try and ensure enclosures and cavities within the HyZero tanks are unlikely to trap liquid • Use of venting systems for flushing • Insulating fuel systems and equipment • Protection of all system sections by safety devices e.g., burst disks and safety valves • Monitor internal system pressure with related emergency procedures, e.g., system depressurisation.
Buoyancy Gas accumulation	• Provide ventilation • Monitoring of hydrogen concentration, pressure, leak detection and evacuation systems
Flammability Ignition, spontaneous combustion Person being caught in a hydrogen flame	• Venting/disposal of unwanted gaseous H_2 through the top of the HyZero tanks • UV or IR flame detection • Inerting of lines before and after system venting • Activation of fire extinguishing spray systems in case of flame detection or emergency activation • Operator training concerning risks specific to hydrogen and emergency procedures • Provision of flameproof clothes and personal protective equipment
Low temperature Ice accretion Embrittlement	• Thermal insulation of equipment, pipelines etc. • Anti-/De-icing • Use of compatible materials • Temperature monitoring, periodic inspection and regular de-/anti-icing of equipment • Emergency procedures in case of operating loss of equipment e.g., blocked valve
Small dimensions of molecule Leak at interface level	• Minimize interfaces and mechanical joints • Use advanced seals • Perform regular helium tightness tests • Hydrogen detection near interfaces that may leak • System redundancy enabling isolation of a leaking system

Table 3-6 identifies relevant hazards and measures for mitigation. In the left column, the properties (black) and the resulting dangers (blue) are listed. Additional hazards, as well as a detailed description of fuel system safety precautions, are listed in Appendix D. Despite all precautions, accidents can occur. According to [85], disk burst, bird strike, emergency landings, and fire protection must be taken into account. Damage to the tank in the event of a disk burst or bird strike is unlikely with HyZero, due to the positioning of the tank. The routing of lines in potential impact areas is mostly avoided. If routing through at-risk areas is unavoidable, the lines are structurally reinforced and equipped with valves that interrupt the supply from the tank. Safety-relevant pipes are designed redundantly. In the event of a crash landing, tanks located in the fuselage are less likely to be damaged [82]. By positioning the tank in the rear of the fuselage, it is structurally secured from both the front and the bottom. A quick release valve, intended

for fuel dumping in case an emergency landing is required shortly after take-off, is not provided due to the low mass of the hydrogen.

3.5 Technology Readiness Levels of Key Technologies

This section summarises the key technologies and assesses them in terms of their market maturity (see Table). For this purpose, the Technology Readiness Level (TRL) classification according is used [91]. If the technology has a level of 4 or higher, it is considered to be ready for market entry by 2035 [87]. Since this is the case for all chosen technologies, an EIS in 2035 is feasible.

Table 3-7: TRL of key technologies.

Key Technology	TRL	Source
Windowless Fuselage	9	[32]
Lifting Body	5	[86]
Strut Braced Wing/Folding Wing	4	[87], [88]
Morphing Wing	5	[87], [89]
Fuel Cell	8	[90]
Hydrogen Driven Engine	5	[2]
BLI	4	[87]

4 Technical Data

Once the feasibility of an EIS in 2035 is proven, the optimisation of the aircraft's performance is initiated. In this chapter, the mass estimation, the aerodynamic data, and the performance of HyZero that resulted from the optimisation are shown.

4.1 Mass Estimation

Table 4-1 shows the masses of the different components of HyZero. Most of them are calculated by semi-empirical equations, which were derived by HOWE and TORENBEEK [92],[93]. There are no semi-empirical equations for a wing like the one used by HyZero, so the wing mass is adopted from a calculation for a similar aircraft by NASA [50]. This adoption is reasonable, because HyZero is just 13 % lighter than the airplane calculated by NASA. Consequently, the wing of HyZero is lighter than the wing calculated by NASA [50]. Additionally, the wing gains additional mass because of the morphing system, which will increase the wing mass by 25 % [].

Table 4-1: Mass estimation.

Component	Mass [kg]			Mass [kg]	
	HyZero	Ref. Aircraft	Component	HyZero	Ref. Aircraft
Fuselage	9117 [92]	9072 [92]	Design Payload	15750	15750
Wing	9516 [50]	7200 [24]	Block Fuel	1562	6277
Empennage	539 [47]	896 [1]	Σ MTOM	56132	60864
Landing Gear	1736 [93]	2633 [93]			
Propulsion	8801	7913	Pylon	979 [24]	979 [24]
Tanks	1090		Hydrogen Pipes	20	
Flight Systems	4145 [92]	4247 [92]	Main Engines	3320 [24]	3330 [24]
Σ MME	34944	31961	BLI+ Systems	870	
Operating Items	2225 [92]	2225 [92]	Nacelle	2023 [24]	2012 [24]
Furnishings	4651 [93]	4651 [93]	Engine Systems	1589 [24]	1592 [24]
Σ OME	41820	38837	Σ Propulsion	8801	7913

4.2 Aerodynamic Data

For the analysis of aerodynamic effects, several attempts at 3D CFD calculations are made with a detailed 3D model, several simplified versions, and half-meshes. However, due to limitations in the student license, those calculations cannot be performed. Therefore, simplifications are made for drag analysis with estimations based on TORENBEEK [93], using the aircraft analysis tool OpenVSP. For lift analysis, the 2D flow solver MSES are used.

4.2.1 Drag

A key factor in raising HyZero's aerodynamic efficiency is to keep drag at a minimum. To reach that goal, a wide variety of features is incorporated, which are further explained in Chapter 3. Due to the unconventional design, especially regarding the fuselage, a model in the aircraft geometry tool OpenVSP is created for the drag analysis to determine wetted areas more precisely. For friction drag in laminar flow, the Blasius equation is used as described in WHITE [94]. Several equations for turbulent

flow can be found in literature. To compare HyZero to the reference aircraft, the explicit fit equation of SPALDING [95] is used to compute friction drag in turbulent flows of both aircraft.

Figure 4-1 illustrates the design choices of the HyZero concept leading to a small decrease in C_{D0} . $C_{D0,empennage}$ is reduced with the introduction of the V-tail, mainly because of a smaller empennage-fuselage interference drag and in parts also due to a slightly smaller wetted area. Due to the lifting fuselage design, the increase in length caused by tank integration can be kept at a minimum which even leads to a small decrease in $C_{D0,fuselage}$. HyZero features an airfoil that is designed for natural laminar flow (NLF). In standard commercial aircraft, the boundary layer flow is turbulent on almost all of the wetted surface. This results in viscous drag five to ten times larger than that of laminar boundary layers [96]. The NASA/LANGLEY NLF(1)-0215F airfoil is determined as a suitable fit as it provides a high $C_{L,max}$, while maintaining a low C_D over a wide range of C_L. At the flight conditions flown in a standard HyZero mission (see Chapter 6), laminar flow is maintained for 48.83 % of chord length in a calculation with the analysis tool XLFR5. This corresponds with data found by STREIT ET AL. [97], who maintain laminar flow for up to 50 % chord length with an NLF airfoil at Ma 0.78 and Re 1.4E+07. The calculated laminar flow length is therefore assumed for the calculations in the present work, whereas the laminar flow length for the reference aircraft is estimated to be 20 % of the lifting surfaces chord length [24]. Laminar flow helps to keep $C_{D0,wing}$ at a value comparable to the reference aircraft despite an increased wetted area.

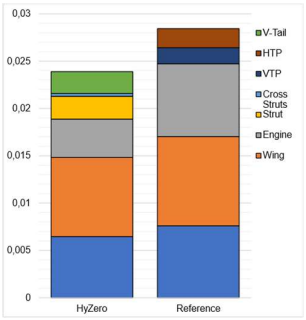

Figure 4-1: Comparison of zero-lift drag coefficient.

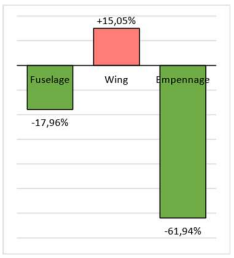

Figure 4-2: Zero-lift drag difference of HyZero compared to the reference aircraft

A visualisation of the difference in zero-lift drag compared to the reference aircraft is given in Figure 4-2. The morphing wing concept, as introduced in Section 'Morphing Wing', further reduces the overall drag coefficient by approximately 3.7 % [98]

The drag share for the lifting body fuselage is determined to 27 % of overall drag (see Figure 4-1). The BLI propulsor, positioned at the rear of the fuselage, ingests the lower 40 % of the boundary layer, equalling to 65 % of the momentum deficit of the fuselage due to the nonlinear velocity curve of a typical boundary layer [70]. At $C_{L,cruise}$, the ratio of viscous drag to total drag is 83 % (see Figure 4-3Figure 4-). This results in a power saving coefficient of 4 % according to Steiner [99], which can roughly be translated into an equal overall drag reduction.

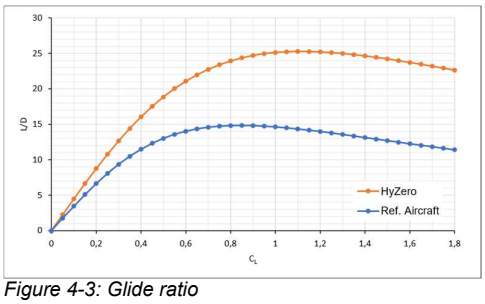

Figure 4-3: Glide ratio

As elaborated in Section 3.3.1, the high aspect ratio of HyZero's wing also reduces lift-induced drag. From Figure 4-3 it can be deducted that the glide ratio of HyZero already exceeds that of the reference aircraft at very low values of C_L. However, the glide ratio finds its maximum at $C_L = 1.1$, which is much higher than $C_{L,cruise} = 0.5$. This could be explained with the high aspect ratio. In the course of optimisation, it was considered to lower the aspect ratio. However, even for significantly lower aspect ratios, which have their $(L/D)_{\max}$ at values closer to $C_{L,cruise}$, the glide ratio of HyZero at $C_{L,cruise}$ exceeds the ones of lower aspect ratios substantially. This shows that the HyZero concept is superior to others even in non-optimal flight conditions. To fully utilize its potential, it could be considered to fly at a lower speed. For reasons of the assignment requirements, this is not explored further in this report. Overall, HyZero can achieve an increase in L/D at $C_{L,cruise}$ of 28.15 % and an increase in $(L/D)_{\max}$ of 58.95 %.

The drag for both HyZero and the reference aircraft is visualised in Figure 4-4. Figure 4-5 shows the total drag of the HyZero concept for different angles of attack.

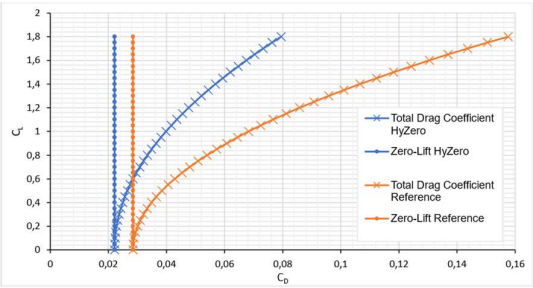

Figure 4-4: Drag polars.

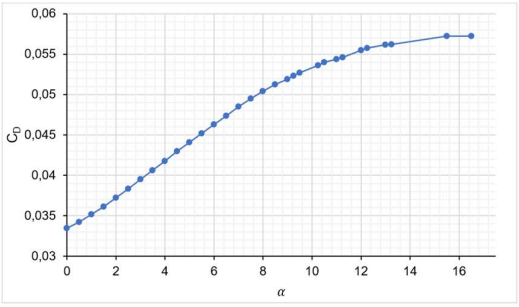

Figure 4-5: Drag coefficient vs. angle of attack.

4.2.2 Lift

As discussed above, an airfoil for natural laminar flow is used for the wing. For computing a $C_L - \alpha$ curve, the airfoil's behaviour is analysed at HyZero's average chord length of 2.58 m with a Reynolds number of Re = 6.78E+06 at Mach 0.7 with MSES. To apply the 2D data to the behaviour of a 3D wing, usually 2D-3D transformations have to be made. Based on investigations by BUSEMANN [100], the simple sweep theory provides transformation rules for infinite swept wings with $C_{L,3D} = f(C_{L,2D}, \varphi_{ref})$. As a finite, tapered wing is considered for the HyZero concept, a reasonable choice would have to be made for φ_{ref} in dependence of the location of flow separation as described by BOPPE [101]. However, the sweep of HyZero's wing is rather small, which is why, $C_{L,3D}$ would not differ significantly. For that reason, 3D transformation is neglected.

Lift is also increased by the lifting fuselage design. The contribution of fuselage lift to the total lift coefficient can be estimated to 20 % of overall lift as investigated by DRELA [29]. The overall calculated lift coefficient of wing and fuselage can be seen in Figure 4-6. The reference aircraft's lift curve can be found in Section 2.2.

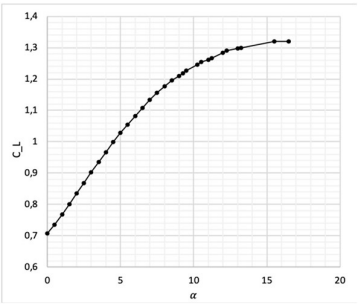

Figure 4-6: Lift coefficient vs. angle of attack.

The hight-lift system is sized according to [24], [102] and CS-25.125 [3] to achieve a reference speed V_{ref} of 130 kt and a take-off field length (TOFL) of less than 2,000 m. HyZero can achieve V_{ref} at MTOM for safety reasons (cf. Section 3.4.4). The high-lift system comprises of a droop nose or nose flaps at the leading edge and a plain flap at the trailing edge. It is assumed that the lifting body provides 19.2 % of the lift in high-lift configuration. In landing configuration HyZero uses a 25° slat and 35° flap deflection angle to achieve a lift coefficient $C_L = 2.226$.

4.3 Aircraft performance

The payload-range diagram of both aircraft retains its characteristic design as seen in Figure 4-7. However, the maximum payload of both aircraft is not much higher than their design payloads. As MTOM is calculated as the sum of OME, block fuel mass and design payload and the MTOM is selected at the design point. The block fuel mass of both aircraft is relatively low and therefore there is little room for the trade-off between fuel mass and payload. By comparison, the CSR-01 maximum payload is 47 % higher than the design payload. For both aircraft, the maximum payload is selected such that a range of 500 km is protected. The ferry range of both aircraft is very close together. While HyZero has a ferry range of 3,302 km, the reference aircraft has 3,296 km.

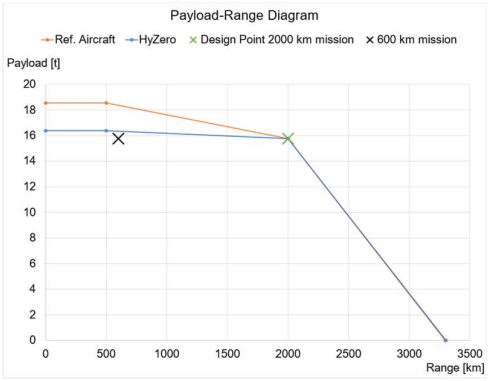

Figure 4-7: Payload-range diagram.

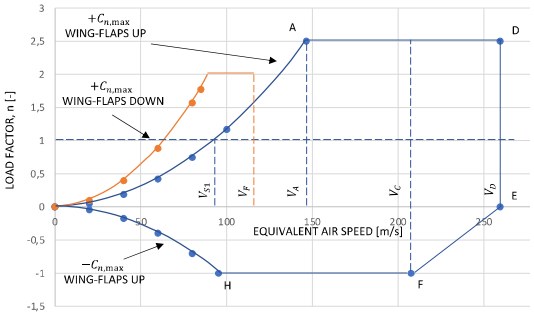

Figure 4-8: V-N diagram.

The V-N diagram created according to Section 'CS 25.333 Flight Manoeuvring Envelope' of the CS-25 Regulations [3] can be seen in .All data is referenced to sea level. According to [3], the equivalent 1g stall speed V_{s1} is defined as the intersection of the line $n = 1$ with the $C_{L,max}$ curve in the diagram. The flight range is limited by the maximum lift coefficient $C_{L,max}$. The following applies:

$$n = \frac{C_{L,max}\,\rho\,S}{2\,W}\,v^2. \tag{4-1}$$

The stall speed is calculated with (4-1) to $92.63\,\frac{m}{s}$. The design manoeuvre speed V_A results from V_{s1}. It can be chosen by the manufacturer but must be at least

$$V_A = \sqrt{2.5}\,V_{s1} = 146.46\,m/s. \tag{4-2}$$

Point A marks the intersection of the $C_{L,max}$ curve with the n_{max} line. According to CS-25 [3] n_{max} is 2.5. The design cruise speed V_c is specified by the requirements. For the design dive speed V_D, a conservative estimation is carried out via (4-3).

$$V_D = 1{,}25\,V_C = 259.47\ m/s \tag{4-3}$$

Analogous to the positive load factor results the point H. According to CS-25 [3], the negative load factor is limited to $n = -1$. The following restrictions apply to fully extended flaps: The speed $V_{S1,extended\ flaps}$ shall be set to at least

$$V_{S1,extended\ flaps} < 1.6\,V_{S1} = 148.21\,m/s. \tag{4-4}$$

The load factor shall be $n = 2$.

All take-off and landing distances of both HyZero and the reference aircraft are calculated using formulas from [35] according to CS 25.111 [3]. For the TOFL the Accelerate Stop Distance (ASD) in dry conditions is determined. For HyZero an ASD of 1,553.5 m is achieved. According to the TLARs the TOFL is set at 2,000 m. Therefore, HyZero has a margin of 28.74 % for wet conditions which is deemed acceptable. This safety margin is further increased as reverse thrust can be used in wet conditions. A selection of results is presented in Table 4-2.

Table 4-2: Take-off and landing performance

		HyZero	Ref. Aircraft	Unit
T/O	Take-Off Distance	1,097.7	1,091.9	[m]
	TOFL 1 engine inop.	1,553.5	1,641.9	[m]
	V_1	61.8	68.0	[m/s]
Landing	Base Distance	980.3	1,067.8	[m]
	66.67 % safety margin dry	1,633.9	1,779.6	[m]
	92 % safety margin wet	1,882.2	2,050.1	[m]

5 Airport and Hydrogen Infrastructure

The introduction of radically new aircraft designs comes with a number of operational challenges. Among the most severe ones is the need for airport infrastructure to be adapted to accommodate the new models. This problem is exacerbated for low-volume aircraft designs, as in that case adapting their infrastructure is even less economically attractive for airport operators. Hydrogen aircraft in particular present additional challenges, since they might require an entirely new fuel procurement chain, infrastructure, and procedures.

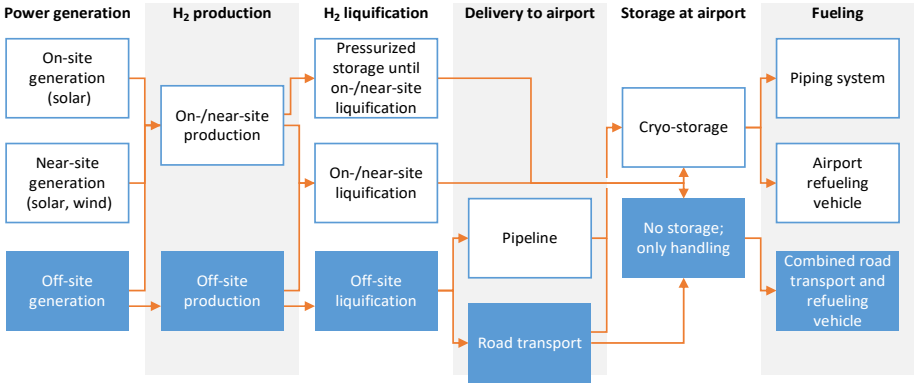

Figure 5-1: Potential and selected liquid hydrogen procurement chain.

In addition to being environmentally friendly and low-cost, HyZero's is designed with the goal of being 'low-friction' for airport operators by largely avoiding the above issues. HyZero is designed to fit within current gate operations without requiring major changes to infrastructure or procedures. The hydrogen procurement chain is developed from the options listed in Figure 5-1 with the goal of requiring the least investment and adjustments from airport operators. The path highlighted in blue is selected.

In the following sections, the assumptions and calculations supporting the selected hydrogen procurement chain are detailed. First, a bottom-up approach is used to determine the total cost of hydrogen based on data available from literature. Secondly, a total energy assessment is made using a top-down approach, based on the efficiency data provided in the Design Challenge problem specification. All costs are in EUR2035 unless specified otherwise, assuming a 2 % annual inflation between 2021 and 2035 as targeted by the European Central Bank [94]. If sources do not specify whether they use real or nominal values, assumptions are made based on context.

5.1 Power Generation

To achieve the least environmental impact, HyZero is powered entirely by 'green' hydrogen, i.e. hydrogen produced exclusively with energy from renewable sources and zero associated emissions as defined by the German Federal Government [103]. To encourage the production of green hydrogen, the Federal Government has decided to provide extensive incentives to industrial electrolysers. Starting on January 1, 2022, industrial producers of green hydrogen are exempt from the EEG surcharge, which was 0.06756 EUR_{2020}/kWh in 2020 [103], [104]. Electrolysers are also exempt from the German electricity tax of 0.0205 EUR_{2020}/kWh [105] and are being reimbursed for the grid charge, which is largely set by the Federal Government and amounted to 0.0264 EUR_{2020}/kWh for industrial customers in 2020 [106], in the first 20 years of their operations. Charges and levies linked to the grid charges constitute the final component of surcharges. They comprise the combined-heat-and-power levy ('KWKG-Umlage'), the concession fee, charges according to Section 19 of the Electricity Grid Charges Ordinance ('StromNEV'), the offshore grid levy, and the levy for switchable loads [107]. Of these, electrolysers are exempt only from the combined-heat-and-power levy with the remaining charges amounting to 0.00763 EUR_{2020}/kWh in 2020 [104]. Combined with the average price for industrial electricity acquisition and sale of 0.0615 EUR_{2020}/kWh in 2020 [104], this puts the price of electricity for electrolysers at 0.06913 EUR_{2020}/kWh post-EEG exemption. Since many exemptions are only granted to large-scale electrolysers, the construction of on-site or near-site power generation was not deemed beneficial considering the high capital expenditure (CapEx) requirements of building solar and wind power sources [103]. The electricity from 100 % renewable sources necessary for the production of green hydrogen are instead sourced from the open market.

The development of electricity prices for industrial consumers until 2035 is subject to great uncertainty. Assuming the exemptions for electrolysers detailed above remain in place, electricity prices for electrolysers in 2035 largely depend on the cost of acquisition and sale of green electricity. This cost is being influenced by several, sometimes conflicting megatrends, including the increasing demand from transportation and industry electrification, the lower operational cost of renewable power sources, changes in population size, the cost of emission certificates, and the improvement of grid and large-scale storage technologies. [108] Price predictions range from a nearly constant cost of acquisition and procurement to a twofold increase until 2035 [109], [110]. Given the ever-decreasing cost of electricity from renewable sources, which is HyZero's sole source, and the expressed intend of the German Federal Government to keep electricity prices for the generation of hydrogen low, the price of -electricity for electrolysers is therefore assumed to remain constant at 0.06913 EUR_{2020}/kWh or 0.093 EUR_{2035}/kWh until 2035 [111].

5.2 Hydrogen Production

Since the government incentives mentioned above only apply to large-scale electrolysis plants and these also offer efficiency improvements over smaller facilities, the hydrogen for HyZero's operation is produced a centralised, off-site location [103], [112]. 40 % of the roughly 50 million tons of hydrogen currently being produced and consumed every year are by-products of industrial process, while 60 % are from dedicated production. Of the latter, around 95 % are produced using carbohydrates and are therefore not green hydrogen. [113] For HyZero, only hydrogen produced from electrolysis is considered. In this process, water is split into hydrogen and oxygen using electricity and one of three process variants: alkaline electrolysis (AEL), polymer electrolyte membrane electrolysis (PEMEL), or high-temperature electrolysis (HTEL) [107]. The technology readiness levels (TRL) of these technologies are 9, 6-8, and 5-6, respectively [107], [114].

AEL as the process with the highest TRL is the technique of choice for producing hydrogen on an industrial scale today and features the lowest production costs [115]. Drawbacks include the purity of the produced hydrogen, with at 99.90 % does not fulfil the requirements of modern fuel cells and necessitates an additional filtering step, and the limited ability of the process to adapt to a fluctuating electricity supply from renewable sources. [116], [117]

PEMEL is less well-established, but seen as having a higher potential for future improvement [118], including significant efficiency, compactness, and production capacity advantages over AEL [119]–[121]. In addition, the resulting hydrogen purity of 99.99 % removes the need for additional filtering [116]. PEMEL offers significant synergies in combination with green electricity from renewable sources: PEMEL can dynamically adapt its production rate and power demand between 0 % and 300 % of nominal power rating, far exceeding the capabilities of AEL and HTEL [117]. It therefore offers the potential for demand-side management, which is seen as an important factor in realizing the transformation of global energy supplies to 100 % renewable sources [122].

HTEL is currently the least developed alternative of the three electrolysis processes. Prototypes are being operated in laboratory environments and only a few, small-scale demonstrators have been implemented. The advantages of HTEL are its high efficiency, reduced CapEx, and its ability to be operated 'in reverse' to produce electricity from hydrogen. [113], [123] Drawbacks include HTEL's inability to flexibly adjust its output as to avoid thermal cycling, the still unknown purity of the hydrogen produced on an industrial scale, and, most importantly, the uncertainty regarding its availability for large-scale hydrogen production in 2035 given its relatively low TRL [115], [120]. Because of these uncertainties and its incompatibility with the fluctuating power output of sustainable sources of energy, the option of using HTEL is dismissed and excluded from the following cost calculations.

When comparing the economics of AEL and PEMEL, initial investment, cost of electricity, maintenance, and electrolysis stack renewal cost are major cost components that need to be considered. All cost components can be annualized over the expected lifetime of the plant, according to the equations in Appendix E [124]. Using a real discount rate of i = 0.04 and an expected lifetime of both AEL and PEMEL systems of N = 23 years [121], the common capital recovery factor is CRF = 0.067. The detailed calculations for the net present cost are shown in Appendix F. They assume initial investment costs of around 500 EUR_{2017}/kW_{el} for large-scale AEL and 700 EUR_{2017}/kWh_{el} for large-scale PEMEL plants in 2035, which equates to around 700 EUR_{2035}/kWh and 980 EUR_{2035}/kWh, respectively [120]. The largest electrolysis plant currently in operation was recently installed in Canada with a power level of 20 MW [125]. The average electrolysis plant suppling HyZero in 2035 is assumed to have a nominal power of 100 MW, based on literature, detailed plans by European companies, and a call for proposals by the European Commission [126]–[128]. Annual maintenance and operations costs are estimated at 22 EUR_{2035} and 8 EUR_{2035} per kW of installed power per year for a 100 MW AEL and PEMEL plant, respectively [115]. The lifetime of the individual electrolysis stacks is estimated as 60,000 and 50,000 hours, respectively, which represents the lower end of the range given by SMOLINKA ET AL. [115] to avoid the losses in efficiency caused by voltage degradation [129]. The capacity factors are 90 % and 70 % for AEL and PEMEL, respectively. The values are chosen to account for the high TRL of AEL and the key advantage of PEMEL, which lies in its ability to change its power level according to the supply of renewable energy.

Table 5-1: Net present cost in 2035, annualized cost & production cost per kg of hydrogen.

	NPC (2035)	Annualized cost	Annual production	Production cost per kg_{H2}
AEL	1,204,930,700 EUR_{2035}	80,730,400 EUR_{2035}	20,124,320 kg_{H2}	4.01 EUR_{2035}
PEMEL	973,990,100 EUR_{2035}	65,257,300 EUR_{2035}	14,731,530 kg_{H2}	4.43 EUR_{2035}

Table 5-1 summarises the calculated results for net present cost (NPC), annualised cost, and cost per kg of hydrogen. The cost per kg of hydrogen is determined by dividing the annualised cost by the annual production, which is determined from the electrolysis plant's installed power, using the equation in Appendix G. The electric power and capacity factors are given above. The lower heating value of hydrogen is LHV_{H2} = 33.3 kWh/kg_{H2}. The system efficiency of AEL and PEMEL electrolysis is 85 % and 80 %, respectively [113].

AEL delivers a 9 % cost advantage over PEMEL in terms of cost per kilogram of hydrogen. However, PEMEL's major advantage is its compatibility with electricity from variable, renewable sources. This compatibility is represented within the calculations in the form of the significantly lower capacity factor and is responsible for a significant part of PEMEL's cost disadvantage. The ability to use the electricity from variable renewable sources guarantees that HyZero's hydrogen is truly 'green'. PEMEL therefore provides the best balance between ecology, cost, and technology-specific advantages for implementation in 2035 and is selected as the optimal technology for producing HyZero's hydrogen. It

is important to note, however, that HyZero's reliance on centralised, off-site production means that HyZero's operators are only one of many purchasers of a site's hydrogen output and have therefore limited influence on the production technology used. Nevertheless, it appears that PEMEL plays a significant role in hydrogen production by 2035, given the advantages listed above.

5.3 Hydrogen Liquification

Similar to hydrogen production, large-scale, centralised hydrogen liquification offers efficiency and cost advantages over a local, on-site process and is therefore selected for HyZero's hydrogen procurement chain [112]. Current state-of-the-art industrial liquification plants require 10 – 20 kWh/kg_{H2}, with 6 kWh/kg_{H2} as a future benchmark [112], [130]. 9 kWh/kg_{H2} is chosen as a reasonable estimate for a large-scale liquification plant in 2035. Small installations suffer from significant reductions in efficiency and exponentially higher specific investment costs, making on-site liquification at the airport unfeasible [112]. The specific cost of hydrogen liquification is calculated using the equation in Appendix H. CONELLY ET AL. estimate a specific cost of investment and operations of around $c_{spec,I\&O} = 1.40\ USD_{2018}/kg_{H2} \approx 1.19\ EUR_{2018}/kg_{H2}$ for liquification plants with a production capacity of 27,000 kg_{H2}/day in California in 2018 [130]. The investigated PEMEL plant's annual production of 14,731,530 kg_{H2} translates into around 40,000 kg_{H2} per day. Assuming this to be the output of a liquification plant directly connected to the PEMEL plant, and considering the fact that the plant is built in Germany instead of California, as well as the likelihood of further technological improvement until 2035, a specific cost of investment and operations of the liquification plant of 1.00 EUR_{2035}/kg_{H2} is a reasonable assumption.

Using the aforementioned specific energy demand of $e_{spec,liq} = 9\ kWh/kg_{H2}$ and the estimation for the cost of green electricity in 2035 from Section 5.1, $c_{el,green} = 0.093\ EUR_{2035}/kWh$, the specific cost of liquification is calculated to $c_{spec,liq} = 1.84\ EUR_{2035}/kg_{H2}$.

5.4 Hydrogen Delivery to the Airport

The hydrogen produced and liquified off-site needs to be delivered to the airports from which HyZero operates. The use of pipelines is dismissed because of the high capital and operation expenditures (OpEx) required for the installation and operation of an infrastructure of the required scale. While a significant expansion of existing compressed hydrogen grids seems feasible until 2035, the same cannot be said for a liquid hydrogen grid because of the significantly higher costs and operational requirements. [131]

Instead, HyZero relies on hydrogen being delivered by cryogenic trucks, which can utilize existing, proven technologies and be scaled easily as HyZero expands to more airports. To further reduce HyZero's environmental impact, these trucks are hydrogen-powered. Transporting cryogenic hydrogen via diesel-powered trucks is well established. Existing cryogenic semi-trailers carry up to 4,000 kg of hydrogen for up to 4,000 km. [132]–[134] Assuming a strong improvement in fuel cell technology for trucking, OOSTDAM estimates long-term reduction of total cost of ownership (TCO) of hydrogen-powered trucks to 0.935 EUR_{2019}/km or 1.31 EUR_{2035}/km [135]. However, in contrast to the regular semi-trailers investigated by OOSTDAM, the cost of a hydrogen-powered liquid hydrogen trailer is impacted significantly by the cost of the hydrogen cargo tank, which is estimated at 650,000 USD_{2035} or approximately 550,000 EUR_{2035} [133]. Including this cost as well as another 10% for auxiliary equipment such as a pumps and fuelling hoses in the TCO calculation model utilized by OOSTDAM yields a higher TCO of approximately 2.00 EUR_{2035}/km for HyZero's specific use case, assuming a 10% residual value consistent with the assumptions by OOSTDAM [135].

Currently, only a single industrial-scale liquification plant exists in Germany. The distance from this plant in Leuna to each major airports in Frankfurt, Hamburg, Munich, and Berlin is between 200 and 400 km. While an increase in liquification plants in Germany until 2035 seems inevitable, the number remain likely limited due to the benefits of large-scale liquification. For the calculation of transportation cost, a distance of 200 km at the low end of this range is therefore assumed. Assuming a conservative average speed of the truck of 50 km/h and hourly personnel cost of 25 EUR_{2035}, the cost of the driver for the 400 km roundtrip is $c_{driver} = 200\ EUR_{2035}$. Once at the airport, the truck is transferred to airport personnel.

Three HyZeros are assumed to be stationed at selected airports at initial deployment in 2035. Each performs an average of 4.3 flights (2.05 flights at 2000 km and 2.25 flights at 600 km) and, therefore, requires 3,504 kg_{H2} of taxi and trip fuel per day. On average, daily hydrogen requirements per airport therefore amount to 10,512 kg_{H2}. This requires three trips by hydrogen-delivery trucks, each filled with an average of 3,504 kg_{H2}. The boil-off in a truck is 0.3% per day or 0.0125% per hour and needs to be considered when filling the truck at the liquification plant [133]. Transportation time is conservatively estimated at four hours, and another hour is included for possible additional delays. Since the delivery

trucks are used to directly fuel the HyZeros, they remain at the airport until they have dispensed their fuel completely. With an average demand per flight of around 817 kg_{H2}, each truck is involved in five fuelling operations, on average. Assuming the average 12.9 HyZero flights per airport per day to be equally spaced between 5:30 am and 11 pm, this means each truck must remain at the airport for an average of six hours and 45 minutes. Another five hours of storage time within the truck are included for potential departure delays, as only a negligible number of flights in the EU are delayed by more than 300 minutes [136]. This puts the maximum boil-off duration at 16.75 hours, which equals a maximum boil-off of 0.2% or around 7 kg_{H2}. This puts the average total hydrogen mass per delivery at 3,511 kg_{H2}. However, the additional 7 kg_{H2} are not considered when calculating the specific delivery cost, as in most cases, they are not used to fuel HyZero but rather remain inside the truck and are recycled at the liquification plant. More significant are the transfer losses, which are also discussed in the next section and amount to an average of 70 kg_{H2} per truck, putting the total amount of hydrogen used for calculating the specific cost of transportation at 3,574 kg_{H2}. [137] The calculations according to the equation given in Appendix I yield a final specific cost of transportation of 0.28 EUR_{2035}/kg_{H2}.

5.5 Fuelling and Gate Operations

To match the 21 minute refuelling time of an A319neo, the delivery trucks' equipment must have the ability to dispense the 1,129 kg_{H2} of taxi and trip fuel required for the 2,000 km trip within 16 minutes, allowing five minutes for installation and removal of the necessary equipment. [139] If more than the taxi and trip fuel are consumed on a given flight, the refuelling process is allowed to take longer. The required liquid hydrogen flow rate is therefore 1.18 kg_{H2}/s. A standard liquid hydrogen trailer dispenses its hydrogen content at about 0.4 kg_{H2}/s [133]. The required flow rate for fuelling HyZero can therefore be achieved by installing two dispenser systems per truck, each with a slightly increased flow rate of 0.59 kg_{H2}/s, and supplying one compartment of HyZero's tank. Low-pressure transfer pumps on the market today already almost provide the necessary flow rate with neglectable heat transfer [137]. Their cost was already considered in the delivery truck TCO calculations.

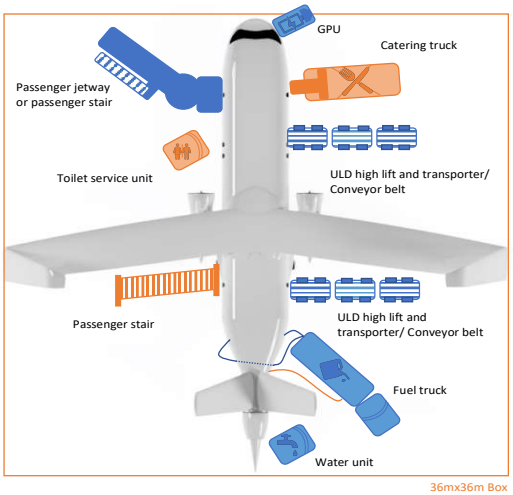

Figure 5-2: Ramp layout according to [138].

The only remaining, significant source of hydrogen boil-off is transfer loss from the receiving tank, which for a transfer process using low-pressure transfer pumps amounts to about 2 % and is considered in the DOC calculations [137]. To minimize the environmental and cost impact of this significant boil-off, it is recovered from the tank compartments' pressure release vents and fed into the fuel cell powering the delivery and fuelling truck, using the red hose shown in Figure 5-2. This reduces the pressure against which the pumps have to work and thereby their power demand, and generates some of the energy required for pumping. [137]

Other than that, gate operations require little adjustments from airport operators as shown in Figure 5-2. Just like with kerosene-fuelled aircraft, fuelling of HyZero can only begin once passengers have deplaned the aircraft, and must be completed before new ones get on board. Other turnaround processes like catering, cleaning, cargo loading, and water servicing can take place in parallel, as hydrogen aircraft handling is not expected to be more dangerous, especially considering the technological advances until 2035. [82], [139]

In its wingtips-up configuration, HyZero falls within the wingspan limit of 36 m for Code C aircraft set by ICAO Annex 14 [41], allowing it to access more airports and utilize existing infrastructure for ground operations. By keeping the main engines below the wings and the BLI engine in the aft section, existing infrastructure can be utilized for maintenance.

During the night, the unused diversion fuel from the final flight of the day must remain in HyZero's tank. This avoids excessive thermal cycling and drastically reduces the need for tank components to cool down during the first fuelling process in the morning, which would lead to additional, significant boil-off. [137] Boil-off from the night is fed into the delivery truck during the next fuelling process, as described above.

5.6 Permanent Infrastructure at the Airport

To minimize the challenges for airport operators in the face of the initial low-volume deployment of HyZero, foregoing the installation of significant hydrogen storage capacities at the airport is a major design decision, resulting in reduced CapEx, OpEx, and safety requirements. Instead, the trucks delivering the hydrogen to the airport are equipped with direct fuelling capabilities.

Building storage capacity for fuels would be associated with significant costs. For major airports, IATA recommends to maintain kerosene storage capacity of around three days' worth of demand [140]. Considering HyZero's anticipated flight schedule, this would equate to around 30 tons of liquid hydrogen storage capacity at each airport. Liquid hydrogen is stored in insulated and cooled cryogenic tanks. Installation cost estimates per kWh of capacity vary widely, from 27 EUR_{2021}/kgH_2 for a 300 ton tank to 680 EUR_{2021}/kg_{H2} for a 270 kg tank and 3,200 EUR_{2021}/kg_{H2} for a 100 kg tank [141], [142]. By fitting a linear curve to the double-logarithmic representation of these numbers, we can estimate a cost of 90 EUR_{2021}/kg_{H2} for our 30 ton tank, putting the total cost per airport at around 2.66 million EUR_{2035} if we assume price reductions from technological improvements to be balanced with inflation.

The NPC calculations detailed in Appendix J show that installing this storage capacity would increase the cost of hydrogen by only around 0.08 EUR_{2035}/kg. However, the initial investment would need to be borne by airport operators. In addition, storing large amounts of liquid hydrogen at the airport would introduce significant safety implications and require the installation of a safety parameter according to the Seveso Directive in the EU [143]. Active cooling and maintenance of the tanks would cause additional operating expenses. These factors combined would significantly increase the friction for airport operators to give HyZero access.

Changes that cannot be avoided is the installation of additional venting in hangars for maintenance, and the implementation of additional training and procedures for the safe handling of hydrogen, due to its volatility. [143]

5.7 Total cost of hydrogen procurement and efficiency assessment

Table 5-2 lists the cost components of HyZero's hydrogen, given the calculations and assumptions detailed above. Since an aircraft operator would not be operating the H_2 production, liquification, and delivery infrastructure himself, a 10 % markup on the total cost is assumed to account for supplier margins. This puts the total specific cost of hydrogen for HyZero's operation at 7.21 EUR_{2035}/kg_{H2}.

Table 5-2: Summary of specific cost components of HyZero's hydrogen.

	H_2 production	H_2 liquification	H_2 delivery	Sum	Total w/ markup
Specific cost	4.43 EUR_{2035}/kg_{H2}	1.84 EUR_{2035}/kg_{H2}	0.28 EUR_{2035}/kg_{H2}	6.55 EUR_{2035}/kg_{H2}	7.21 EUR_{2035}/kg_{H2}

For the total energy assessment, a top-down approach, based on the efficiency values provided by the Design Challenge problem specification, is utilized. The efficiency of electrolysis is given as $\eta_{electrolysis} = 0.80$, and that of liquification, distribution, and storage, which is assumed to include fuelling, as a combined $\eta_{liq,distr,sto} = 0.85$. Since the electricity for hydrogen production and liquification is from renewable sources, the efficiency of electricity generation is $\eta_{el} = 1$. The total onboard efficiency from hydrogen tank to thrust in cruise is shown to be around $\eta_{onboard} = 0.43$, neglecting the impact of the fuel cell and BLI engine. The total efficiency of the hydrogen chain from electricity generation to thrust is therefore approximately $\eta_{total} = 0.29$.

6 Operational Aspects

After establishing the configuration of HyZero and evaluating novel operational aspects which arise from the use of liquid hydrogen, HyZero's mission is optimised with regard to climate impact, energy consumption, and noise. This this chapter evaluates both reference missions. For certain aspects, like determining the required tank size, the block fuel is relevant which includes the trip fuel and all reserves, as defined by EU-OPS 1.255 [144]. However, the block fuel including reserves does not represent fuel consumption in daily operations, and is therefore not suitable for economic evaluation. Instead, these are based on trip fuel, which excludes reserves.

6.1 Flight Path Optimisation

While HyZero does not emit any CO_2 or CO (cf. Section 3.4) during its flight, its emission of H_2O and thus the potential to produce contrails is greatly increased compared to kerosene-fuelled aircraft. In addition, NO_x is emitted, albeit at reduced levels. Noise emissions also remain an issue for HyZero. The level and impact of these emissions is greatly influenced by HyZero's flight path. Both the 600 km and

2,000 km design missions are designed to be as environmentally friendly as possible. In addition, the economic viability of the 2000 km mission and lifecycle aspects are investigated.

6.1.1 Climate Impact from GHGs

To reduce the climate impact of both design missions, the greenhouse gas (GHG) emissions of HyZero are studied. Counterintuitively, GHG emission and climate impact can show an inverse correlation. For example, at lower altitudes, HyZero has a higher fuel consumption and thus emits more H_2O, but nevertheless has a lower climate impact due to the atmospheric effects. GHG emissions are calculated and used to determine HyZero's climate impact, which can be measured using several different metrics. [143] The CO_2-equivalent (CO_2-eq) metric is chosen, as it has a the most reliable values readily available. CO_2-eq is calculated by multiplying each GHG emission with its respective global warming potential (GWP) and adding them all up to obtain the total CO_2-eq or climate impact. GWP represents which amount of CO_2 would have the same time-integrated radiative forcing (RF) as the GHG under consideration. For this work a time horizon of 100 years is chosen, which is widely accepted as a standard [63]. It should be kept in mind that this does not necessarily indicate the same effect on climate change. [145] However, uncertainty increases with increasing relevance. While GHG emission can be well quantified their climate change potential is not as certain. [146] CO_2-eq is seen as an appropriate balance between the two. Calculations are based on figures given by SVENSSON ET AL. [63].

The standard cruising altitude of aircraft the size of HyZero is between FL 330 and 360. Decreasing an aircraft's cruising altitude can greatly reduce the CO_2-eq of aircraft fuelled with LH_2 due to the lower GWP with decreasing altitude [63]. However, this change comes with disadvantages in fuel consumption due to the higher density at lower altitudes. This means a trade-off is necessary when choosing the cruising altitude. An investigation into the optimal cruising altitude is conducted for HyZero.

Although studies have argued that contrails produced by aircraft fuelled with LH_2 are less harmful [147] due to being optically thinner among other factors, some studies argue that the climate impact of current contrails is between three [148] and ten times [149] as high as that of GHG emissions. To avoid any harm from contrails it is decided that HyZero flies below FL 300 to produce not any at all [143]. The CO_2-eq and fuel burn is analysed across different FLs as modelled for HyZero. The CO_2-eq from GHG emissions is already greatly reduced below FL300 and NO_x is the only remaining GHG which possesses a GWP. Although the GWP of NO_x continues to decrease below FL 330 the fuel consumption continues to rise, meaning reductions in CO_2-eq come to a hold. Therefore, the cruising altitude of HyZero is set at FL 290, as this is the cruising altitude with no contrail formation and least fuel consumption.

6.1.2 Noise

Aircraft noise is relevant during take-off, climb and landing. It is investigated in three phases, namely emission when it is created by the aircraft, transmission where it propagates, and immission where the person is impacted. To measure noise, several different metrics are used. For ICAO chapter 14 regulations, the Effective Perceived Noise Decibel (EPNdB) of a pre-defined flight path is used. It is a measure of perceived noise integrated over time. In Germany noise protection zones are defined based on equivalent noise levels L_{Aeq}, which consider the intensity and frequency of aircraft noise for a specific location. However, for HyZero the DLR dose-response relation is chosen as the defining metric. [150] It is established to consider flight events that wake residents from their sleep as it is shown that existing metrics based solely on acoustics does not transfer into the right conclusions to improve the health of residents. [150] It is outside the scope of this paper to calculate noise levels on the ground, but the reasoning from [150] is used to guide the design of the flight path.

While HyZero uses state-of-the-art engines to reduce noise emissions, the flight path is optimised as well. When designing the flight path, a trade-off between speed and altitude has to be made. For departure a Modern Noise Abatement (MoNA) Procedure which has shown to reduce the 90 db(A) noise footprint the most in a review of different departure procedures and is therefore used by HyZero. [151] For the approach HyZero uses a Continuous Descent Approach (CDA). A CDA reduces noise emissions and fuel burn (and thus GHG emissions). The noise footprint can be substantially reduced and 25 – 40 % of fuel saved during final approach when using a CDA. [152] During a CDA, the aircraft flies at idle power setting and burns less fuel therefore but also flies at lower speeds. This traditionally reduces airport capacity, but recent studies show that this drawback can be eliminated [153].

6.2 Overall Energy Analysis

The design goal of HyZero is to make the 600 and 2,000 km reference missions as environmentally friendly as possible. Additionally, the economic viability of the 2,000 km mission is investigated. The calculation of the total energy consumption is conducted for the block fuel of the 600 km mission and 2,000 km mission. Additionally, the duration of each mission segment is computed. In Table 6-1 the

outcome of the overall energy consumption calculation is presented together with the duration of every flight segment. The taxi and reserve segments are the same for both missions. Due to the low fuel mass penalty of LH_2 the reserve segments of both missions have very similar energy requirements which appear identical due to rounding. Through the configuration decisions detailed in previous chapters, HyZero consumes between 50 and 70 % less energy on every mission evaluated. Including all reserves, HyZero requires 1,561.5 kg of block fuel on the 2,000 km mission. This is the dimensioning figure for the tank size. The fuel masses for all missions are summarised in Table 6-2.

Table 6-1: Total critical mission energy consumption.

		2,000 km mission		600 km mission	
	Mission segments	Duration [min]	Energy [MWh]	Duration [min]	Energy [MWh]
HyZero	Taxi-out	12	3.3	12	3.3
	Contingency	5	1.6	5	0.6
	Climb out	25	4.8	25	4.7
	Cruise	132	26.8	23	7.0
	Descent	16	0.3	16	0.3
	Missed approach + Climb	5	0.9	5	0.9
	Alternate Cruise	22	4.1	22	4.1
	Alternate Descent	3	0.1	3	0.1
	Final Reserve	30	5.4	30	5.4
	Additional fuel	15	3.0	15	3.0
	Taxi-in	8	1.8	8	1.8
	TOTAL, Block	268	52.0	158	31.2
	TOTAL, Trip	196	37.6	87	17.8
Ref. Aircraft	TOTAL, Block	256.4	88.3	155.5	50.2
	TOTAL, Trip	188	63.2	87	27.0
	Saving, Block [%]	-4.3	69.8	-1.6	60.9
	Saving, Trip [%]	-4.1	68.1	0.0	51.7

Table 6-2: Overview of fuel masses.

	2,000 km mission		600 km mission	
	Trip Fuel [kg]	Block Fuel [kg]	Trip Fuel [kg]	Block Fuel [kg]
HyZero	1,129.17	1,561.5	533.67	936.8
Ref. Aircraft	4,777.1	6961.8	2,130.8	4,183.3

Additionally, the climate impact of both reference missions is determined with methods described in Section 6.1.1. The climate impact is not investigated for reserve segments as this is not part of the standard operating procedure, but only for segments which are included in the trip fuel. As these are the same missions which form the basis of the DOC calculation the trip fuel additionally includes the taxi fuel and a delay of 15 minutes on 20 % of flights is included to achieve more robust results. The result is presented in Figure 6-1. It is evident that HyZero has an extremely low climate impact.

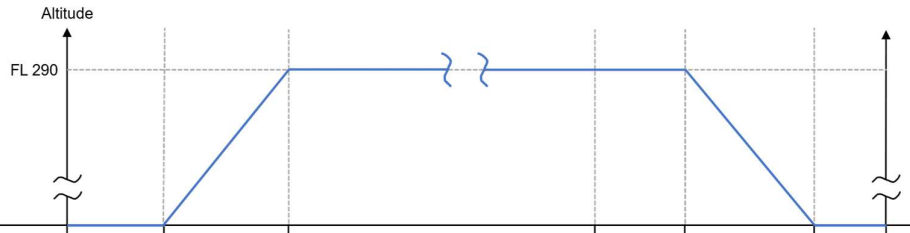

Segment	Taxi-out	Climb	Cruise	15 minute delay	Descent & landing	Taxi-in	TOTAL
CO2-eq 2000 km	-5.1	-8.3	656.0	14.9	-0.3	-2.8	654.3
CO2-eq 600 km	-5.1	-8.3	165.7	14.9	-0.3	-2.8	164.04

Figure 6-1: CO_2-eq of both reference missions.

As laid out in Section 3.1, HyZero does not utilise removable tanks to realise weight reductions for the shorter 600 km mission, as the drawbacks outweigh the benefits. This design decision opens up an opportunity aligned with HyZero's mission of accessing a growing number of airports without requiring significant CapEx or OpEx from airport operators. HyZero's standard operating model of delivering hydrogen to airports via trucks already minimises the friction for operators. However, some airports may not be accessible this way. Alternatively operators could trial new HyZero routes without committing to significant investment. If these airports are within 600 km of an airport with refuelling capabilities, they can be serviced by HyZero by utilising its entire tank capacity designed for the 2,000 km mission. HyZero would carry the return fuel on the outbound flight, removing the need for refuelling at the destination. The capacity is sufficient to allow the aircraft to respect all requirements regarding reserve fuel. HyZero could remain in holding for up to 30 minutes during the outbound flight. Only if this time, which represents

about 30 % of the trip time, is exceeded, HyZero could not operate the return flight. In these rare cases, LH_2 would need to be supplied on-demand. This risk seems acceptable, given the potential for significant expansion of business. The fuel penalty is 0.5 % and it is therefore seen as a viable option for future operators.

6.3 DOC Analysis

Throughout the DOC analysis, both mission distances are used to create more realistic operations. Aircraft generally do not operate exclusively on either a 600 or 2,000 km mission. Therefore HyZero's block time and daily flight numbers are matched with the average of all US narrowbodies [154]. In 2019, these had an average daily block time of 9.95 hours and operated 4.3 daily flights. This leads to a daily frequency of 2.05 and 2.25 of the 2,000 and 600 km mission, respectively, for HyZero. This results in an average HyZero mission distance of 1,266.6 km.

The DOC analysis is carried out based on the same method as employed by CeRAS [155]. All costs are presented in EUR_{2035}. Unless otherwise specified the same input values are used for the DOC as those set out in [155]. If costs change with the type of flight and/or region, an international flight within the EU is assumed. The average mission is used for all DOC calculations of HyZero and the reference aircraft to achieve comparability. All formulas are adjusted to account for any changes in aircraft configuration. For the price of hydrogen fuel the price calculated in Chapter 5 at 7.21 EUR_{2035}/kg is used. To account for boil-off losses during fuelling 2 % of fuel consumption is added.

A price of 0.69 EUR_{2035}/L for JET A-1 [156] is assumed and 2.64 EUR_{2035}/L for SAF [157]. With a 30 % SAF blend this leads to a fuel price of 1.60 EUR_{2035}/kg for the reference aircraft. The fuel costs of the reference aircraft are supplemented by the cost of CO_2 pricing. The price of CO_2 emissions is projected at 112.2 EUR_{2035}/t_{CO2} under the EU-Emissions Trading Scheme (EU-ETS). [158] The price of both aircraft is estimated using [47] and calibrated with a A319neo from [159]. This results in a list price for HyZero of 95.6 $mEUR_{2035}$ and 102.0 $mEUR_{2035}$.

The results of the DOC Analysis are presented in Figure 6-2 and supplemented in Appendix E. It can be seen that total DOC of HyZero are significantly higher due to the high fuel costs. For both aircrafts the fuel costs make up the majority of DOC. A sensitivity analysis shows that a 20 % decrease in the price of LH_2 decreases the total DOC of HyZero by 14.2 %. Additionally the total DOC of the reference aircraft would rise by 25.4 % if it was only fuelled with SAF. Another observation is that HyZero has lower fees, as they are directly correlated to the aircraft's MTOM. Although HyZero has a lower list price its capital costs are higher nonetheless due to the BLI propulsor. This explains the rise in maintenance costs as well.

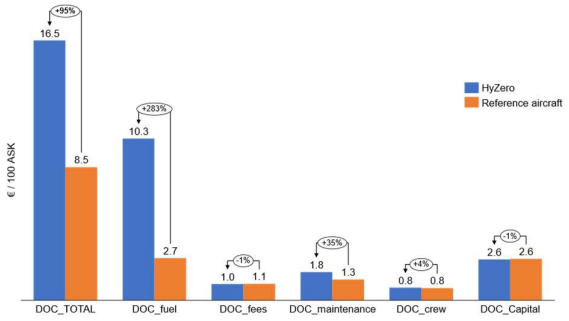

Figure 6-2: DOC comparison.

Overall, the DOC of both HyZero and the reference aircraft are greatly influenced by political and macro-economic factors and thus the projected DOC are expected to change with changing circumstances. At this point in time hydrogen prices appear prohibitively high, which should change with advances in hydrogen production technology. Further it has been proposed by the EU Commission to price non-CO_2 emissions as well in the future [1]. Unlike the reference aircraft, HyZero emits very little non-CO_2 emissions. This means such pricing would impact the reference aircraft extremely negatively compared to HyZero. This is also the reason for the increased maintenance cost.

6.4 Lifecycle aspects

While HyZero is very environmentally friendly in flight, the impact of hydrogen procurement and the production of the aircraft itself cannot be disregarded. HyZero strives for minimal environmental impact through the exclusive use of electricity from 100 % renewable sources in its hydrogen procurement chain. However, even green electricity has a non-zero emission intensity, mostly due to emissions caused during production and installation of capacity. For quantifying the emissions, a roughly 49-51 split of electricity from renewable sources between wind and solar power in 2035 [160], and emission intensities of 11 g CO_2-eq/kWh and 44 g CO_2-eq/kWh for electricity from wind and solar, respectively [161], are assumed. In Section 5.7, the total efficiency of the hydrogen chain from electricity generation to thrust is calculated to be $\eta_{total} = 0.29$. The 817.2 kg of hydrogen required for the average HyZero flight, which contain around 27.2 MWh of energy, therefore require 93.8 MWh of electricity. Given the above

split between wind and solar, and the emission intensities, total emissions from hydrogen procurement for the average HyZero flight are 2,610 kg CO_2-eq. Likewise, the reference aircraft's SAF is not CO_2-neutral either, and only reduced CO_2 emissions by 80 %. With the average flight of the reference aircraft requiring 3,483 kg of fuel, this equates to 647.8 kg of CO_2 just for the SAF production. Due to the large variety of SAFs, it is outside the scope to include other GHG emissions, which do arise.

Both manufacturing and end-of-life uses of HyZero possess the same drawbacks as conventional, state-of-the-art aircraft using CFRP components. Although progress is being made towards enabling the recycling of CFRP, it is unclear at what point in time the processes will have matured enough. [162]

7 Conclusion

As required by the problem formulation of the NASA/DLR Design Challenge 2021, HyZero carries 150 passengers over a maximum distance of 2,000 km and thus competes with other short- to medium-haul aircraft. For this reason, HyZero is compared with an updated CeRAS CSR-01 with improved engines, whose fuel consumption is extrapolated for use in 2035, as a suitable reference aircraft. This includes a mass estimation and comparison of the necessary system components between the two aircraft.

The HyZero configuration has a high aspect ratio wing supported by a strut. This provides reductions in fuel consumption. The two main engines, which burn hydrogen in the combustion chamber, are located under the wing, which is mounted on the fuselage. In addition, a boundary layer ingesting fan at the end of the fuselage sucks in the boundary layer, increasing the propulsive efficiency. Other striking features of the HyZero include a V-tail and a windowless fuselage, resulting in reduced fuel consumption through mass savings. In addition, the wings are designed to be foldable in order to be handled at conventional 36 m airport boxes. The use of morphing wings leads not only to a reduction in drag, but also to a reduction in noise.

Greenhouse gas emissions are decreased significantly compared to the reference aircraft. The main reason for this is the use of hydrogen as fuel, with its entire procurement chain being focused on sustainability. The hydrogen is produced at a central, off-site location by electrolysis from water and green electricity, so that no fossil resources are consumed in its production. In flight, the hydrogen is converted into thrust by combustion in engines. In addition, a fuel cell system is used to supply electrical energy to systems and the BLI fan. Through these two types of energy conversion, only NO_x and water vapor are released. Due to the well thought-out HyZero concept, few structural changes to the airport infrastructure are necessary.

In addition, the HyZero configuration reduces noise emission. To achieve this, noise-generating components are optimised for noise reduction, which include the engines, the morphing wings, and the wetted surfaces, such as the fuselage, wings, and tail unit. Finally, the noise level on the ground is reduced by a modified flight path during the climb and landing approach. Since HyZero's economical operation is highly dependent on fuel prices and government decisions, there is some uncertainty associated with the economic viability of the concept in 2035, although recent developments in political and public debate are promising.

HyZero meets the TLARs of the NASA/DLR Design Challenge 2021, making it an environmentally friendly alternative for air transport in 2035.

8 References

[1] European Commission, ‘Communication from the Commission to the European Council, the European Economic and Social Committee and the committee of the regions’, Brüssel, 2019.

[2] DLR, ‘White Paper Zero Emission Aviation’. Meinders + Elstermann GmbH & Co. KG, 2020.

[3] EASA, *Certification Specifications for Large Aeroplanes (CS-25). Amendment 26*. 2020.

[4] K. Risse, ‘ILR MICADO Design of CeRAS CSR-01 Technical Report’. ILR, 2014.

[5] F. Schültke, B. Aigner, T. Effing, P. Strathoff, and E. Stumpf, ‘MICADO: Overview of Recent Developments within the Conceptual Aircraft Design and Optimization Environment’, 2021, doi: 10.25967/530093.

[6] N. Herbig, *Nutzwertanalyse: eine Methode zur Bewertung von Lösungsalterativen und zur Entscheidungsfindung*. Norderstedt: Books on Demand, 2016.

[7] T. Ritchey, ‘General Morphological Analysis’, *R Bak. T Barnes J Beck Eds Proc. 1st Int. Conf. Educ. Data Min. Pp 8–17*, vol. Swedish Morphological Society, 2013.

[8] F. Zwicky and A. G. Wilson, ‘New Methods of Thought and Procedure: Contributions to the Symposium on Methodologies’, 1967. doi: 10.1007/978-3-642-87617-2.

[9] J. Andersson and S. Grönkvist, ‘Large-scale storage of hydrogen’, *Int. J. Hydrog. Energy*, vol. 44, no. 23, pp. 11901–11919, 2019, doi: 10.1016/j.ijhydene.2019.03.063.

[10] A. Colozza and L. Kohout, ‘Hydrogen Storage for Aircraft Applications Overview’, 2002.

[11] E. Rivard, M. Trudeau, and K. Zaghib, ‘Hydrogen Storage for Mobility: A Review’, *Materials*, vol. 12, p. 22, 2019, doi: 10.3390/ma12121973.

[12] T. Brunner, O. Kircher, and M. Kampitsch, ‘Cryo-Compressed Hydrogen Storage’, in *Fuel Cells : Data, Facts and Figures*, John Wiley & Sons, Ltd, 2016, pp. 162–174. doi: 10.1002/9783527693924.ch17.

[13] Thanh et al., ‘Technical Assessment of Compressed Hydrogen Storage Tank Systems for Automotive Applications’, Argonne National Laboratory - Nuclear Engineering Division, Chicago, ANL-10/24, 2010.

[14] H.-W. Pohl, ‘Hydrogen and other alternative fuels for air and ground transportation’, 1995.

[15] Airbus S.A.S., ‘These pods could provide a blueprint for future hydrogen aircraft’, 2020. https://www.airbus.com/newsroom/stories/hydrogen-pod-configuration.html (accessed Jun. 17, 2021).

[16] N. S. Dangi and A. V. Patel, ‘Simulated Drag Study of Fuel Tank Configurations for Liquid Hydrogen-Powered Commercial Aircraft’, *SAE Int. J. Sustain. Transp. Energy Environ. Policy*, vol. 1, no. 2, pp. 153–166, 2020, doi: 10.4271/13-01-02-0010.

[17] G. D. Brewer and R. E. Morris, ‘Tank and Fuel Systems Considerations for Hydrogen Fueled Aircraft’, *SAE Trans.*, pp. 3088–3103, 1975.

[18] G. D. Brewer, *Hydrogen aircraft technology*. Routledge, 1991.

[19] D. Verstraete, P. Hendrick, P. Pilidis, and K. Ramsden, ‘Hydrogen fuel tanks for subsonic transport aircraft’, *Int. J. Hydrog. Energy*, vol. 35, no. 20, pp. 11085–11098, 2010, doi: 10.1016/j.ijhydene.2010.06.060.

[20] C. Winnefeld, T. Kadyk, B. Bensmann, U. Krewer, and R. Hanke-Rauschenbach, ‘Modelling and Designing Cryogenic Hydrogen Tanks for Future Aircraft Applications’, *Energies*, vol. 11, no. 1, Art. no. 1, 2018, doi: 10.3390/en11010105.

[21] P. Sharke, ‘H2 tank testing’, *Mech. Eng.-CIME*, vol. 126, no. 4, pp. 20–21, 2004.

[22] D. Verstraete, ‘The potential of liquid hydrogen for long range aircraft propulsion’, 2009.

[23] G. D. Brewer, R. E. Morris, G. W. Davis, E. F. Versaw, and G. R. Cunnington Jr., ‘Study of fuel systems for LH2-fueled subsonic transport aircraft’, Lockheed-California Co., Burbank, Technical Report N-78-31085, 1978.

[24] E. Stumpf, *Vorlesung Flugzeugbau II Sommersemester 2021*. 2021.

[25] V. Mukhopadhyay, J. Welstead, J. Quinlan, and M. D. Guynn, 'Structural Configuration Systems Analysis for Advanced Aircraft Fuselage Concepts', presented at the AIAA Modeling and Simulation Technologies Conference, Washington, D.C., 2016. doi: 10.2514/6.2016-4419.

[26] IATA, 'Technology Roadmap for Environmental Improvement'. 2020.

[27] A. Velicki and D. Jegley, 'PRSEUS Development for the Hybrid Wing Body Aircraft', presented at the AIAA Centennial of Naval Aviation Forum '100 Years of Achievement and Progress', Virginia Beach, VA, Sep. 2011. doi: 10.2514/6.2011-7025.

[28] J. T. Chambers, B. M. Yutko, R. Singh, and C. Church, 'Structural Optimization Study of the D8 Double-Bubble Composite Fuselage', Grapevine, Texas, 2017. doi: 10.2514/6.2017-0508.

[29] M. Drela, 'Development of the D8 Transport Configuration', presented at the 29th AIAA Applied Aerodynamics Conference, Honolulu, Hawaii, 2011. doi: 10.2514/6.2011-3970.

[30] A. H. Bowers, O. J. Murillo, B. Eslinger, J. Technology, and C. Gelzer, 'On Wings of the Minimum Induced Drag: Spanload Implications for Aircraft and Birds', p. 22, 2016.

[31] A. L. Habermann, A. Gokhale, and M. Hornung, 'Numerical investigation of the effects of fuselage upsweep in a propulsive fuselage concept', *CEAS Aeronaut. J.*, vol. 12, no. 1, pp. 173–189, 2021, doi: 10.1007/s13272-020-00487-2.

[32] S. Steinke, 'Emirates führt virtuelle Fenster ein', *Flugrevue*, 2017.

[33] S. Bagassi, F. Lucchi, and F. Persiani, 'Aircraft Preliminary Design: a windowless concept', no. 211, p. 7, 2015.

[34] M. C. Moruzzi and S. Bagassi, 'Preliminary design of a short-medium range windowless aircraft', *Int. J. Interact. Des. Manuf. IJIDeM*, vol. 14, no. 3, pp. 823–832, 2020, doi: 10.1007/s12008-020-00676-7.

[35] E. Stumpf, *Vorlesung Flugzeugbau I Wintersemester 2020/21*. 2021.

[36] J. D. Anderson, *Fundamentals of aerodynamics*, 2nd ed. New York: McGraw-Hill, 1991.

[37] M. K. Bradley, C. K. Droney, and Allen, Timothy J., 'Subsonic Ultra Green Aircraft Research: Phase II – Volume I – Truss Braced Wing Design Exploration', National Aeronautics and Space Administration, Boeing Research and Technology, Huntington Beach, 2015.

[38] J. D. Anderson, *Introduction to flight*, Eighth edition. New York, NY: McGraw-Hill Education, 2016.

[39] V. Rozov, A. Hermanutz, C. Breitsamter, and M. Hornung, 'Aeroelastic Analysis of a Flutter Demonstrator With a Very Flexible High-Aspect-Ratio Swept Wing', 2017.

[40] Yarygina, M. V. and Popov, Yu. I., 'Development of the Weight Formula for a Folding Wing', Moscow Aviation Institute (State Technical University), Moscow, 2011.

[41] International Civil Aviation Organization (ICAO), 'Annex 14 to the Convention on International Civil Aviation - Volume I, Aerodrome Design and Operations', 2020.

[42] Federal Aviation Administration, *Special Conditions: The Boeing Company Model 777-8 and 777-9 Airplanes; Folding Wingtips*. 2018, p. 4. Accessed: Jul. 10, 2021. [Online]. Available: https://www.federalregister.gov/documents/2018/05/18/2018-10576/special-conditions-the-boeing-company-model-777-8-and-777-9-airplanes-folding-wingtips

[43] B. Woods and M. Friswell, 'Preliminary Investigation of a Fishbone Active Camber Concept', in *ASME 2012 Conference on Smart Materials, Adaptive Structures and Intelligent Systems, SMASIS 2012*, 2012, vol. 2. doi: 10.1115/SMASIS2012-8058.

[44] D. P. Raymer, *Aircraft design: a conceptual approach*. Reston, VA: American Institute of Aeronautics and Astronautics, Inc, 2018.

[45] B. K. Woods, O. Bilgen, and M. I. Friswell, ‘Wind tunnel testing of the fish bone active camber morphing concept’, *J. Intell. Mater. Syst. Struct.*, vol. 25, no. 7, pp. 772–785, 2014, doi: 10.1177/1045389X14521700.

[46] J. Delfs and L. Enghardt, ‘Latest research on the reduction of aircraft noise at the source’, presented at the ICANA, Frankfurt, 2013.

[47] A. K. Kundu, M. Price, and D. Riordan, *Conceptual aircraft design: an industrial approach*. Hoboken, NJ: John Wiley & Sons, 2019.

[48] P. E. Purser and J. P. Campbell, ‘Experimental verification of a simplified vee-tail theory and analysis of available data on complete models with vee tails’, 1945.

[49] J. Roskam, *Airplane design*. Lawrence, Kan: DARcorporation, 1997.

[50] M. Bradley and C. K. Droney, ‘Subsonic Ultra Green Aircraft Research Phase II: N+4 Advanced Concept Development’, 2012.

[51] N. Dyantyi, A. Parsons, C. Sita, and S. Pasupathi, ‘PEMFC for aeronautic applications: A review on the durability aspects’, *Open Eng.*, vol. 7, no. 1, pp. 287–302, 2017.

[52] G. Oliveira, L. G. Trapp, and A. Puppin-Macedo, ‘Engine-Airframe Integration Methodology for Regional Jet Aircrafts with Underwing Engines’, in *41st Aerospace Sciences Meeting and Exhibit*, American Institute of Aeronautics and Astronautics, 2003. doi: 10.2514/6.2003-934.

[53] M. Hoogreef, R. Vos, R. de Vries, and L. L. Veldhuis, ‘Conceptual Assessment of Hybrid Electric Aircraft with Distributed Propulsion and Boosted Turbofans’, in *AIAA Scitech 2019 Forum*, American Institute of Aeronautics and Astronautics, 2019. doi: 10.2514/6.2019-1807.

[54] T. Hecken *et al.*, ‘Conceptual Design Studies of “Boosted Turbofan” Configuration for short range’, in *AIAA Scitech 2020 Forum*, American Institute of Aeronautics and Astronautics, 2020. doi: 10.2514/6.2020-0506.

[55] National Academies of Sciences, Engineering, and Medicine, *Commercial Aircraft Propulsion and Energy Systems Research: Reducing Global Carbon Emissions*. 2016. doi: 10.17226/23490.

[56] L. Wiart, O. Atinault, R. Grenon, B. Paluch, and D. Hue, ‘Development of NOVA aircraft configurations for large engine integration studies’, in *33rd AIAA Applied Aerodynamics Conference*, 2015, p. 2254.

[57] D. Giesecke, M. Lehmler, J. Friedrichs, J. Blinstrub, L. Bertsch, and W. Heinze, ‘Evaluation of ultra-high bypass ratio engines for an over-wing aircraft configuration’, *J. Glob. Power Propuls. Soc.*, vol. 2, pp. 493–515, 2018, doi: 10.22261/JGPPS.8SHP7K.

[58] D. Daggett, S. Brown, and R. Kawai, ‘Ultra-efficient Engine Diameter Study Ultra-efficient Engine Diameter Study’. 2003.

[59] R. von der Bank *et al.*, ‘Compressors for ultra-high-pressure-ratio aero-engines’, *CEAS Aeronaut. J.*, vol. 7, no. 3, pp. 455–470, 2016, doi: 10.1007/s13272-016-0200-9.

[60] A. H. Epstein, ‘Aeropropulsion for Commercial Aviation in the Twenty-First Century and Research Directions Needed’, *AIAA J.*, vol. 52, no. 5, pp. 901–911, 2014, doi: 10.2514/1.J052713.

[61] F. Lou and N. L. Key, ‘Design Considerations for the Final-Stage Centrifugal Compressor in Aeroengines’, *J. Propuls. Power*, vol. 36, no. 5, pp. 791–795, 2020, doi: 10.2514/1.B37522.

[62] R. Faaß, ‘Cryoplane: Flugzeuge mit Wasserstoffantrieb’, *Airbus Dtschl. Cryoplane Present.*, 2001.

[63] F. Svensson, A. Hasselrot, and J. Moldanova, ‘Reduced environmental impact by lowered cruise altitude for liquid hydrogen-fuelled aircraft’, *Aerosp. Sci. Technol.*, vol. 8, no. 4, pp. 307–320, 2004, doi: 10.1016/j.ast.2004.02.004.

[64] B. Khandelwal, A. Karakurt, P. R. Sekaran, V. Sethi, and R. Singh, ‘Hydrogen powered aircraft : The future of air transport’, *Prog. Aerosp. Sci.*, vol. 60, pp. 45–59, 2013, doi: 10.1016/j.paerosci.2012.12.002.

[65] H. Lei and B. Khandelwal, 'Investigation of Novel Configuration of Hydrogen Micromix Combustor for Low NOx Emission', in *AIAA Scitech 2020 Forum*, American Institute of Aeronautics and Astronautics, 2020. doi: 10.2514/6.2020-1933.

[66] J. Kurzke and I. Halliwell, *Propulsion and power: an exploration of gas turbine performance modeling*. Springer, 2018.

[67] I. P. Van Dijk, A. G. Rao, and J. P. Van Buijtenen, 'Stator Cooling and Hydrogen Based Cycle Improvements', *Int Soc Air Breath. Engines 2009*, pp. 2009–1165, 2009.

[68] A. J. Jackson, 'Optimisation of aero and industrial gas turbine design for the environment', Cranfield University, 2009.

[69] A. Seitz *et al.*, 'Proof of Concept Study for Fuselage Boundary Layer Ingesting Propulsion', *Aerospace*, vol. 8, no. 1, Art. no. 1, 2021, doi: 10.3390/aerospace8010016.

[70] J. Welstead and J. L. Felder, 'Conceptual design of a single-aisle turboelectric commercial transport with fuselage boundary layer ingestion', in *54th AIAA aerospace sciences meeting*, 2016, p. 1027.

[71] A. Uranga *et al.*, 'Boundary Layer Ingestion Benefit of the D8 Transport Aircraft', *AIAA J.*, vol. 55, no. 11, pp. 3693–3708, 2017, doi: 10.2514/1.J055755.

[72] P. Giannakakis, Y.-B. Maldonado, N. Tantot, C. Frantz, and M. Belleville, 'Fuel burn evaluation of a turbo-electric propulsive fuselage aircraft', in *AIAA Propulsion and Energy 2019 Forum*, American Institute of Aeronautics and Astronautics, 2019. doi: 10.2514/6.2019-4181.

[73] L. Wiart and C. Negulescu, *Exploration of the Airbus Nautilius Engine Integration Concept*. 2018.

[74] L. López de Vega, G. Dufour, and N. Garcia Rosa, 'Fully Coupled Body Force–Engine Performance Methodology for Boundary Layer Ingestion', *J. Propuls. Power*, vol. 37, no. 2, pp. 192–201, 2021.

[75] J. Bijewitz, A. Seitz, and M. Hornung, 'Power Plant Pre-Design Exploration for a Turbo-Electric Propulsive Fuselage Concept', in *2018 Joint Propulsion Conference*, American Institute of Aeronautics and Astronautics, 2018. doi: 10.2514/6.2018-4402.

[76] R. H. Jansen, M. L. Celestina, and H. D. Kim, 'Electrical Propulsive Fuselage Concept for Transonic Transport Aircraft', 2019.

[77] W.-R. Canders, J. Hoffmann, and M. Henke, 'Cooling Technologies for High Power Density Electrical Machines for Aviation Applications', *Energies*, vol. 12, no. 23, Art. no. 23, 2019, doi: 10.3390/en12234579.

[78] V. A. Sethuraman and J. W. Weidner, 'Analysis of sulfur poisoning on a PEM fuel cell electrode', *Electrochimica Acta*, vol. 55, no. 20, pp. 5683–5694, 2010.

[79] J. Kallo, G. Renouard-Vallet, M. Saballus, G. Schmithals, J. Schirmer, and K. A. Friedrich, 'Fuel cell system development and testing for aircraft applications', in *18th world hydrogen energy conference*, 2010, vol. 2010.

[80] M. G. Sürer and H. T. Arat, 'State of art of hydrogen usage as a fuel on aviation', *Eur. Mech. Sci.*, vol. 2, no. 1, pp. 20–30, 2018.

[81] C. M. Benson, P. G. Holborn, A. M. Rolt, J. M. Ingram, and E. Alexander, 'Combined Hazard Analyses to Explore the Impact of Liquid Hydrogen Fuel on the Civil Aviation Industry', in *Volume 3: Ceramics; Coal, Biomass, Hydrogen, and Alternative Fuels*, Virtual, Online, Sep. 2020, p. V003T03A009. doi: 10.1115/GT2020-14977.

[82] U. Schmidtchen and E. Behrend, 'Hydrogen aircraft and airport safety', no. Renewable and Sustainable Energy Reviews, Elsevier, vol. 1(4), pp. 239–269, 1997.

[83] M. J. Sefain, 'Hydrogen aircraft concepts and ground support', Cranfield University, 2005.

[84] D. Silberhorn, G. Atanasov, J.-N. Walther, and T. Zill, 'ASSESSMENT OF HYDROGEN FUEL TANK INTEGRATION AT AIRCRAFT LEVEL', p. 14.

[85] A. Westenberger *et al.*, 'Liquid Hydrogen Fuelled Aircraft – System Analysis (Final Technical Report Cryoplane)', Final report, 2002.

[86] IATA, 'Technology Roadmap for Environmental Improvement'. 2020.

[87] IATA, 'Aircraft Technology Roadmap to 2050 - IATA'. 2020.

[88] D. Wells, 'VSPAERO SUGAR High/Volt TBW Aerodynamic Analysis', p. 13, 2016.

[89] A. Y. N. Sofla, S. A. Meguid, K. T. Tan, and W. K. Yeo, 'Shape morphing of aircraft wing: Status and challenges', *Mater. Des.*, vol. 31, no. 3, pp. 1284–1292, 2010, doi: 10.1016/j.matdes.2009.09.011.

[90] Safran Group, 'Fuel cells: green energy on board', *Safran Group*, 2017. https://www.safran-group.com/media/fuel-cells-green-energy-board-20170405

[91] NASA, 'Technology Readiness Level Defintion', 2021. https://esto.nasa.gov/files/trl_definitions.pdf (accessed Jul. 18, 2021).

[92] D. Howe, *Aircraft conceptual design synthesis*. London: Professional Engineering Pub, 2000.

[93] E. Torenbeek, *Synthesis of subsonic airplane design: an introduction to the preliminary design, of subsonic general aviation and transport aircraft, with emphasis on layout, aerodynamic design, propulsion, and performance*. Delft : The Hague : Hingham, MA: Delft University Press ; Nijhoff ; Sold and distributed in the U.S. and Canada by Kluwer Boston, 1982.

[94] F. M. White, *Fluid mechanics*, 8th ed. McGraw-Hill Education, 2017.

[95] D. B. Spalding, 'A Single Formula for the "Law of the Wall"', *J. Appl. Mech.*, vol. 28, no. 3, pp. 455–458, 1961, doi: 10.1115/1.3641728.

[96] N. Beck, T. Landa, A. Seitz, L. Boermans, Y. Liu, and R. Radespiel, 'Drag Reduction by Laminar Flow Control', *Energies*, vol. 11, no. 1, p. 252, Jan. 2018, doi: 10.3390/en11010252.

[97] T. Streit, S. Wedler, and M. Kruse, 'DLR Natural and Hybrid Transonic Laminar Wing Design incorporating new methodologies', 2014.

[98] B. K. Woods and M. I. Friswell, 'Multi-objective geometry optimization of the Fish Bone Active Camber morphing airfoil', *J. Intell. Mater. Syst. Struct.*, vol. 27, no. 6, pp. 808–819, Apr. 2016, doi: 10.1177/1045389X15604231.

[99] H.-J. Steiner, A. Seitz, Wieczorek, K. Plötner, A. Isikveren, and M. Hornung, *Multi-disciplinary Design and Feasibility Study of Distributed Propulsion Systems*, vol. 1. 2012.

[100] A. Busemann, 'Aerodynamischer Auftrieb bei Überschallgeschwindigkeit', Rome, Italy, 1935.

[101] C. W. Boppe, 'Aircraft drag analysis methods', presented at the Special Course on Engineering Methods in Aerodynamic Analysis and Design of Aircraft, Neuilly-sur-Seine, France, 1992.

[102] D. Scholz, 'High Lift Systems and Maximum Lift Coefficients'. 2015.

[103] Bundesregierung, *Verordnung zur Umsetzung des Erneuerbare-Energien-Gesetzes 2021 und zur Änderung weiterer energierechtlicher Vorschriften*. 2022.

[104] BDEW Bundesverband der Energie- und Wasserwirtschaft e.V., 'BDEW Strompreisanalyse Januar 2021', 2021.

[105] Deutscher Bundestag, *Stromsteuergesetz (StromStG)*. 1999.

[106] WD 5: Wirtschaft und Verkehr, Ernährung, Landwirtschaft und Verbraucherschutz, 'Fragen zur Entwicklung der Netzentgelte im Stromsektor', Documentation WD 5-3000-012/20, 2020.

[107] Deutsche Energie-Agentur GmbH (dena), 'Power to X: Technologien', Berlin, 2018.

[108] E. Panos and M. Densing, 'The future developments of the electricity prices in view of the implementation of the Paris Agreements: Will the current trends prevail, or a reversal is ahead?', *Energy Econ.*, vol. 84, p. 104476, 2019, doi: 10.1016/j.eneco.2019.104476.

[109] Elbe Energie, 'Strompreise: Preisanstieg bis 2030 um 38 % erwartet', *Energie Blog*, 2020. https://www.elbe-energie.de/strompreise-preisanstieg-bis-2030-um-38-erwartet/

[110] M. Haller, C. Loreck, and V. Graichen, ‘Die Entwicklung der EEG-Kosten bis 2035 - Wie der Erneuerbaren-Ausbau entlang der langfristigen Ziele der Energiewende wirkt’, Agora Energiewende, Short study 074/09-S-2015/D, 2015.

[111] MWIDE.NRW, ‘Entwicklung der Strompreise für private und industrielle Verbraucher, mit und ohne staatliche Belastungen’, 2018.

[112] U. Cardella, L. Decker, and H. Klein, ‘Economically viable large-scale hydrogen liquefaction’, *IOP Conf. Ser. Mater. Sci. Eng.*, vol. 171, p. 012013, 2017, doi: 10.1088/1757-899X/171/1/012013.

[113] M. Klell, H. Eichlseder, and A. Trattner, *Wasserstoff in der Fahrzeugtechnik: Erzeugung, Speicherung, Anwendung*, 4., Aktualisierte und erweiterte Auflage. Wiesbaden [Heidelberg]: Springer Vieweg, 2018.

[114] R. Pinsky, P. Sabharwall, J. Hartvigsen, and J. O’Brien, ‘Comparative review of hydrogen production technologies for nuclear hybrid energy systems’, *Prog. Nucl. Energy*, vol. 123, p. 103317, 2020, doi: 10.1016/j.pnucene.2020.103317.

[115] T. Smolinka *et al.*, ‘Industrialisierung der Wasserelektrolyse in Deutschland: Chancen und Herausforderungen für nachhaltigen Wasserstoff für Verkehr, Strom und Wärme’, Bundesministerium für Verkehr und digitale Infrastruktur (BMVI), Berlin, 2018.

[116] K. Görner and D. Lindenberger, ‘Technologiecharakterisierungen in Form von Steckbriefen’, Virtuelles Institut „Strom zu Gas und Wärme“, 2015.

[117] G. Müller-Syring, M. Henel, W. Köppel, H. Mlaker, M. Dr. Sterner, and T. Dr. Höcher, ‘Entwicklung von modularen Konzepten zur Erzeugung, Speicherung und Einspeisung von Wasserstoff und Methan ins Erdgasnetz’, Deutscher Verein des Gas- und Wasserfaches e.V. (DVGW e.V.), Final report G1-07–10, 2013.

[118] Noack et al., ‘Studie über die Planung einer Demonstrationsanlage zur Wasserstoff-Kraftstoffgewinnung durch Elektrolyse mit Zwischenspeicherung in Salzkavernen unter Druck’, Deutsches Zentrum für Luft- und Raumfahrt, Stuttgart, Project report, 2015.

[119] C. C. Kwasi-Effah, A. I. Obanor, and F. A. Aisien, ‘A Review on Electrolytic Method of Hydrogen Production from Water’, *Am. J. Renew. Sustain. Energy*, vol. 1, no. 2, pp. 51–57, 2015.

[120] Roeb et al., ‘Wasserstoff als ein Fundament der Energiewende. Teil 1: Technologien und Perspektiven für eine nachhaltige und ökonomische Wasserstoffversorgung’, DLR, 2020.

[121] A. Regett and C. Pellinger, ‘Power2Gas – Hype oder Schlüssel zur Energiewende?’, *Energiewirtschaftliche Tagesfragen*, no. 10/2014, pp. 79–84, 2014.

[122] J. Aghaei and M.-I. Alizadeh, ‘Demand response in smart electricity grids equipped with renewable energy sources: A review’, *Renew. Sustain. Energy Rev.*, vol. 18, pp. 64–72, 2013, doi: 10.1016/j.rser.2012.09.019.

[123] B. Pitschak, J. Mergel, and M. Müller, ‘Elektrolyse-Verfahren’, in *Wasserstoff und Brennstoffzelle*, J. Töpler and J. Lehmann, Eds. Berlin, Heidelberg: Springer Berlin Heidelberg, 2017, pp. 207–227. doi: 10.1007/978-3-662-53360-4_11.

[124] HOMER Energy, ‘Annualized Cost’, *HOMER Pro 3.14*. 2021. Accessed: Jul. 18, 2021. [Online]. Available: https://www.homerenergy.com/products/pro/docs/latest/annualized_cost.html

[125] T. Grube *et al.*, ‘A techno-economic perspective on solar-to-hydrogen concepts through 2025’, *Sustain. Energy Fuels*, vol. 4, no. 11, pp. 5818–5834, 2020, doi: 10.1039/D0SE00896F.

[126] J. Incer, J. Mörsdorf, T. Morosuk, and G. Tsatsaronis, ‘Hydrogen energy storage – exergy-based analysis of the charging process’, presented at the 6th International Conference on Contemporary Problems of Thermal Engineering (CPOTE 2020), 2020.

[127] E. Taibi, H. Blanco, R. Miranda, and M. Carmo, ‘Green Hydrogen Cost Reduction. Scaling up electrolysers to meet the 1.5°C climate goal’, International Renewable Energy Agency (IRENA), 2020.

[128] European Commission, ‘Horizon 2020 Framework Programme. Develop and demonstrate a 100 MW electrolyser upscaling the link between renewables and industrial applications’. 2020.

[129] L. Bertuccioli, A. Chan, D. Hart, F. Lehner, B. Madden, and E. Standen, 'Study on development of water electrolysis in the EU', E4tech Sàrl with Element Energy Ltd, Lausanne, Final Report, 2014.

[130] E. Connelly, M. Penev, A. Elgowainy, and C. Hunter, 'Current Status of Hydrogen Liquefaction Costs', US Department of Energy, DOE Hydrogen and Fuel Cells Program Record 19001, 2019.

[131] D. Krieg, *Konzept und Kosten eines Pipelinesystems zur Versorgung des deutschen Straßenverkehrs mit Wasserstoff*. Jülich: Forschungszentrum Jülich, 2012.

[132] United States Driving Research and Innovation for Vehicle efficiency and Energy sustainability (U.S. DRIVE), 'Hydrogen Delivery Technical Team Roadmap', Roadmap, 2013.

[133] C. Yang and J. Ogden, 'Determining the lowest-cost hydrogen delivery mode', *Int. J. Hydrog. Energy*, vol. 32, no. 2, pp. 268–286, 2007, doi: 10.1016/j.ijhydene.2006.05.009.

[134] Fischedick et al., 'Shell Hydrogen Study. Energy of the Future? Sustainable Mobility through Fuel Cells and H2', Shell Deutschland Oil GmbH, Hamburg, Study, 2017.

[135] M. Oostdam, 'Techno-economic assessment of a hydrogen fuel-cell tractor semi-trailer. Exploratory research into the feasibility.', Delft University of Technology, Delft, 2019.

[136] C. Walker, 'All-causes delay and cancellations to air transport in Europe. Annual report for 2019.', Eurocontrol, CDA_2019_004, 2020.

[137] G. Petitpas, 'Boil-off losses along LH2 pathway', Lawrence Livermore National Laboratory, Livermore, Technical Report LLNL-TR-750685, 2018.

[138] B. Bauer, 'Herausarbeitung von Optimierungspotenzialen bei der Koordination und Kooperation von am Turn-Around Prozess beteiligten Akteuren', Hochschule Bremen, 2017.

[139] Airbus S.A.S., 'A319. Aircraft Characteristics. Airport and Maintenance Planning'. 2020.

[140] IATA, 'IATA Guidance on Airport Fuel Storage Capacity', Montreal, Edition 1, 2008.

[141] W. A. Amos, 'Costs of Storing and Transporting Hydrogen', National Renewable Energy Laboratory, Golden, Colorado, NREL/TP-570-25106, 1998.

[142] J. Jespen, 'Technical and Economic Evaluation of Hydrogen Storage Systems based on Light Metal Hydrides', Dissertation, Helmut-Schmidt-Universität, Hamburg, 2013.

[143] Fuel Cells and Hydrogen 2 Joint Undertaking., *Hydrogen-powered aviation: A fact based study of hydrogen technology, economics, and climate impact by 2050.* LU: Publications Office, 2020.

[144] European Commission, 'COMMISSION REGULATION (EC) No 8/2008 of 11 December 2007 amending Council Regulation (EEC) No 3922/91 as regards common technical requirements and administrative procedures applicable to commercial transportation by aeroplane'. 2007.

[145] R. K. Pachauri *et al.*, *Climate change 2014: synthesis report. Contribution of Working Groups I, II and III to the fifth assessment report of the Intergovernmental Panel on Climate Change*. IPCC, 2014.

[146] J. S. Fuglestvedt, 'Metrics of Climate Change: Assessing Radiative Forcing and Emission Indices', *Clim. Change*, vol. 58, no. 3, pp. 267–331, 2003, doi: 10.1023/A:1023905326842.

[147] L. Ström, 'First simulations of cryoplane contrails', *J. Geophys. Res.*, vol. 107, no. D18, p. 4346, 2002, doi: 10.1029/2001JD000838.

[148] J. E. Green, 'Air Travel – Greener by Design Mitigating the environmental impact of aviation: Opportunities and priorities', *Aeronaut. J. 1968*, vol. 109, no. 1099, pp. 361–416, 2005, doi: 10.1017/S0001924000000841.

[149] H. Mannstein and U. Schumann, 'Aircraft induced contrail cirrus over Europe', *Meteorol. Z.*, vol. 14, no. 4, pp. 549–554, 2005, doi: 10.1127/0941-2948/2005/0058.

[150] M. Basner, A. Samel, and U. Isermann, 'Aircraft noise effects on sleep: Application of the results of a large polysomnographic field study', *J. Acoust. Soc. Am.*, vol. 119, no. 5, pp. 2772–2784, 2006, doi: 10.1121/1.2184247.

[151] H. Hemmer, M. Schaefer, and T. Otten, ‘Einfluss lärmarmer An- und Abflugverfahren auf NOx- und CO2-Emissionen im Flughafennahbereich’, 2008.

[152] F. Wubben and J. Busink, ‘Environmental benefits of continuous descent approaches at Schiphol Airport compared with conventional approach procedures’, 2000.

[153] P. B. Sinapius and M.-M. Temme, ‘FlexiGuide-flexible ATM in the E-TMA to reduce environmental impacts’, in *2015 IEEE/AIAA 34th Digital Avionics Systems Conference (DASC)*, 2015, pp. 1A2-1.

[154] MIT Global Airline Industry Program, ‘Airline Data Project. Aircraft and Related’, 2020. http://web.mit.edu/airlinedata/www/Aircraft&Related.html (accessed Jul. 15, 2021).

[155] K. Franz, ‘CeRAS Direct Operating Cost (DOC) Model’. 2014.

[156] D. Rutherford, X. S. Zheng, B. Graver, and N. Pavlenko, ‘Potential tankering under an EU sustainable aviation fuels mandate’, 2021.

[157] J. O’Malley, N. Pavlenko, and S. Searle, ‘Estimating sustainable aviation fuel feedstock availability to meet growing European Union demand’. International Council on Clean Transportation, 2021.

[158] Argus Media group, ‘EU ETS price €32-65/t under 2030 scenarios’, 2020. https://www.argusmedia.com/en/news/2142240-eu-ets-price-3265t-under-2030-scenarios (accessed Jul. 16, 2021).

[159] Airbus Media Relations, ‘Airbus Aircraft 2018 Average List Prices’. 2019.

[160] Kemmler et al., ‘Energiewirtschaftliche Projektionen und Folgeabschätzungen 2030/2050’, Bundesministerium für Wirtschaft und Energie, 2020.

[161] Schlömer et al., ‘Annex III: Technology-specific cost and performance parameters’, *Clim. Change 2014 Mitig. Clim. Change Contrib. Work. Group III Fifth Assess. Rep. Intergov. Panel Clim. Change*, 2014.

[162] Q. Sanchez, M. Jones, S. Monir, Y. Vagapov, and S. Lupin junior, ‘Evaluation of Methodology for the Carbon Fibre Recycling’, St. Petersburg and Moscow, Russia, Jan. 2020, pp. 2178–2183. doi: 10.1109/EIConRus49466.2020.9039382.

[163] A. Goldberg, ‘Fahrwerksauslegung im Flugzeugentwurf und Berechnung Bodenbelastung in PresTo’, HAW Hamburg, 2011.

[164] D. C. M. Benson, ‘Safety Challenges and Opportunities for LH2-fuelled aircraft and Supporting Infrastructure’, 2019.

[165] Airbus Deutschland GmbH, ‘Liquid Hydrogen Fuelled Aircraft – System Analysis (Cryoplane)’, 2003.

[166] HOMER Energy, ‘Capital Recovery Factor’, *HOMER Pro 3.14*. [Online]. Available: https://www.homerenergy.com/products/pro/docs/latest/capital_recovery_factor.html

9 Appendix

A. Landing Gear

When designing the landing gear, the lateral stability, the clearance when entering the landing gear bay, the longitudinal check of the tail clearance angle as well as the lateral clearance of the wing have to considered. A check of the engine clearance is not necessarily due to the high wing design.

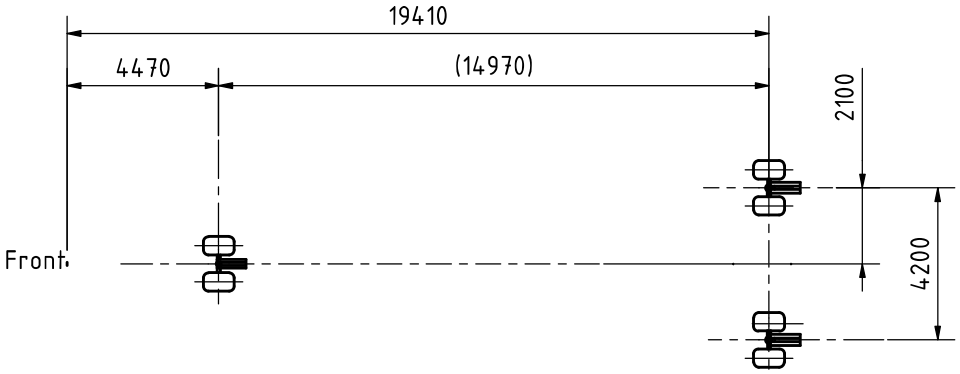

Figure 9-1: Landing Gear Position

The undercarriage is designed in the conventional tricycle layout. The landing gear position is determined by the front/rear or upper CG position and the MAC of the wing. The chassis is integrated after [24], [163] at 34pprox.. 65 % MAC. The tail clearance angle of 12° defined after [24], [163], is checked. The nose gear is positioned according to [24], [163] so that 15 % of the total weight is on the nose gear in the forward CG position and 8 % in the aft CG position. The lateral TSA_{lat} and longitudinal stability TSA_{long} are determined as follows:

$$TSA_{long} = \arctan\left(\frac{x_{Fm} - x_{AFTCG}}{\Delta z_{CG} + H}\right) \geq 15° \tag{9-1}$$

$$TSA_{lat} = 90° - \arctan\left(\frac{H + \Delta z_{CG} + 0{,}5 * \left(d_{fslg} - d_{cabin}\right)}{(D + X)\sin(\alpha)}\right) \leq 55° \tag{9-2}$$

The result is $TSA_{long} = 43.8°$, $TSA_{lat} = 35.5°$. To prevent a wing strike, a minimum bank angle of 6° to 8° is required. HyZero's configuration features a wing tip clearance angle of about 12°. The main aircraft dimensions and characteristics are gathered in Table 3-1.

Table 3-1: HyZero data.

Aircraft	
Length	35.82 m
Height	8.06 m
MTOM	59,063 kg
Wing Area	119 m2
Aspect Ratio	19.55
Anhedral	3°
Sweep Leading Edge	9.16°
Taper Ratio	0.5
Empennage Area	36.37 m2
Take-off Field Length Dry	1,553.5 m
Landing Field Length	980.3 m
Climb Rate	1,700 ft/min
Cruise Speed	Ma 0.7
Cruise Altitude	FL 290
Glide Ratio	18.86

Figure 3-1: General arrangement.

As HyZero is a high-wing aircraft, the main landing gear cannot be accommodated in the wing. For this reason, the landing gear is folded into the fuselage. The landing gear is folded into the structural reinforcement on the lower fuselage, to which the struts are also connected.

B. Derivatives V-Tail

CG-Position	Forward	Design	Aft
$C_{m0,CG}$	0.21780097	0.24909009	0.28633326
$C_{m,CG}$	0.01509458	0.04990524	0.09134007
$C_{n\beta}$	0.22012681	0.21886393	0.21736074
$C_{n,CG}$	0.00922263	0.07289354	0.07276636

C. Boil-off calculation

Assumptions:

- Constant pressure & volume
- Constant heat inflow / outflow
- No mass inflow
- Only Boil-off mass outflow
- Power consumption only by evaporation

- Maximum outer temperature for very hot airport

Description	Equation & Value
Power Balance	$\dot{Q}_{in/out} + P_{cons} = 0$
Heat inflow / outflow	$\dot{Q}_{in/out} = \alpha * S * \Delta T$
Thermal conductivity	$\alpha = 0{,}04\ W/m^2K$
Tank surface	$S = 57{,}92\ m^2$
Temperature difference	$\Delta T = T_{max} + T_{min}$
Maximum Temperature	$T_{max} = 50\ °C = 333.15\ K$
Minimum Temperature	$T_{max} = 20.27\ K$

Power consumption	$P_{cons} = -\Delta h * \dot{m}$
Evaporation enthalpy	$\Delta h = 445{,}5\ kJ/kg$
Boil-off mass flow	$\dot{m} = \frac{\alpha * S * (T_{max} + T_{min})}{\Delta h} = 1{,}63\ g/s$
Fuel mass	$m_{fuel} = 1583\ kg$
Boil-off rate	$f = \frac{\dot{m}}{m_{fuel}} = 9\ \%/day$

D. Hydrogen Hazards

Table 9-1 identifies hazards directly related to liquid hydrogen according to [81], [164]. Since the hydrogen is vaporised during the interaction with the propulsion system or from boil-off, Table 9-2 highlights hazards for the gaseous state. [81]

Table 9-1: Summary of major hazards (liquid hydrogen systems) according to [81]

Hazard categories	Heat management/ transport	Combustion
Temperature	Properties effect	Properties effect
Pressure	Expansion from heat increases, ingress of air forming a flammable atmosphere	Importance of maintaining temperature to support combustion
Chemical	Leaks of flammable materials, and compatibility of materials (e.g., embrittlement).	Leaks of flammable materials, and compatibility of materials (e.g., embrittlement).
Mechanical	System damage from impact, vibration, strain	System damage from impact, vibration, strain, and thermoacoustic oscillation in combustors
Leak/ spill	Flammable hazards from the formation of a flammable atmosphere	Flammable hazards from the formation of a flammable atmosphere
Physiological	Burn (hot)	Burn (hot)
Fire/ Explosion	Confined explosion, danger of deflagration to detonation transition in event of ignition	Flameout risk and ensuring re-ignition, Danger of deflagration to detonation transition in event of ignition

Table 9-2: Summary of major hazards (gaseous hydrogen systems) according to [81]

Hazard categories	Storage	Heat management/ transport
Temperature	Cryogenic hazards to people and equipment, expansion/ damage effects from heat input	Cryogenic hazards to people/equipment, expansion/ damage effects from heat input, the formation of highly flammable hydrogen-oxygen or oxygen 'slush' around leaks/ at cold surfaces.
Pressure	Expansion from heat increases, backflow of contaminated/ higher pressure stream	Expansion from heat increases, ingress of air forming a flammable atmosphere
Chemical	Contamination causing blockages or oxidation, ortho- para conversion causing increased expansion, leaks of flammable/ cryogenic materials, compatibility of materials (e.g.embrittlement).	Contamination causing blockages or oxidation, ortho-para conversion causing increased expansion, leaks of flammable/ cryogenic materials, compatibility of materials (e.g., embrittlement).
Mechanical	System damage from sloshing, Impact, vibration, and strain	System damage from thermoacoustic oscillation of liquid/ gas fuel, fluid-hammer, impact, vibration and strain
Leak/ spill	Cryogenic hazards to people and equipment, flammable hazards from the formation of a flammable atmosphere	Cryogenic hazards to people and equipment, flammable hazards from the formation of a flammable atmosphere
Physiological	Burns (cold, heat), asphyxiation	Burn (cold, heat), asphyxiation

In the following, the fuel system is examined in more detail as it is a safety-critical system. In general, the tank and lines are designed to withstand vibrations as well as mechanical and thermal loads without leakage. To isolate the fuel system from the passenger cabin, lines are routed outside the cabin. Since the tank operates in hot weather conditions, boil-off cannot be avoided economically. In order to not endanger operations, sufficient volume is kept in the tank for expansion. At the highest point of the tank, the gas is led out via an emergency vent system through the tail unit as the highest point of the aircraft, once it reaches a critical pressure. To prevent the air from flowing back or the gas from igniting, a non-return valve and a flame arrester are integrated. Due to the pressure differences, an insulation system is required that is designed according to the fail-safe principle. The pressure relief system must be provided in each isolated volume to avoid large rapid pressure increase. In the HyZero concept, the pumps are designed redundantly and fail-safe. They can be switched off at any time without additional risks. [84], [165]

Critical values such as pressure and temperature are recorded, and warnings are sent to the pilot or co-pilot. Monitoring of the insulation vacuum allows continuous leakage control of lines and connections and automatic initiation of countermeasures in the event of a fault. These measures can be taken completely passively by exploiting the pressure differences in the system or their absence. While checking for leaks is mainly be done by gas detectors, there may be some isolated and gas-tight compartments where pressure sensors could do the same job. The monitoring of leak detection and insulation integrity must be designed to be fail-safe in this case. [83]

E. Annualized Cost and Capital Recovery Factor

Annualized cost [124]:

$$c_{annualised} = CRF * c_{NPC} \tag{9-3}$$

c_{NPC} is the net present cost, i.e. the present value of all costs of installing, maintaining, and operating the electrolysers over their lifetime. CRF is the capital recovery factor which can be calculated from the following equation [166]:

$$CRF = \frac{i * (1+i)^N}{(1+i)^N - 1} \tag{9-4}$$

F. Net Present Cost Calculations of AEL and PEMEL plants

			Nominal cash flow										Discounted cash flow	
			AEL					PEMEL					AEL	PEMEL
Year	Period	Discount Factor	Investment	Electricity	Maintenance	Stack renewal	Sum	Investment	Electricity	Maintenance	Stack renewal	Sum	Sum	Sum
2035	0	1	- 70.000.000,00 €	€ -	- €	- €	- 70.000.000,00 €	- 98.000.000,00 €	- €	- €	- €	- 98.000.000,00 €	- 70.000.000,00 €	- 98.000.000,00 €
2036	1	0,961538462	- €	- 73.321.200,00 €	- 2.200.000,00 €	- €	- 75.521.200,00 €	- €	- 57.027.600,00 €	- 800.000,00 €	- €	- 57.827.600,00 €	- 72.616.538,46 €	- 55.603.461,54 €
2037	2	0,924556213	- €	- 73.321.200,00 €	- 2.200.000,00 €	- €	- 75.521.200,00 €	- €	- 57.027.600,00 €	- 800.000,00 €	- €	- 57.827.600,00 €	- 69.823.594,67 €	- 53.464.866,86 €
2038	3	0,888996359	- €	- 73.321.200,00 €	- 2.200.000,00 €	- €	- 75.521.200,00 €	- €	- 57.027.600,00 €	- 800.000,00 €	- €	- 57.827.600,00 €	- 67.138.071,80 €	- 51.408.525,83 €
2039	4	0,854804191	- €	- 73.321.200,00 €	- 2.200.000,00 €	- €	- 75.521.200,00 €	- €	- 57.027.600,00 €	- 800.000,00 €	- €	- 57.827.600,00 €	- 64.555.838,27 €	- 49.431.274,84 €
2040	5	0,821927107	- €	- 73.321.200,00 €	- 2.200.000,00 €	- €	- 75.521.200,00 €	- €	- 57.027.600,00 €	- 800.000,00 €	- €	- 57.827.600,00 €	- 62.072.921,41 €	- 47.530.071,96 €
2041	6	0,790314526	- €	- 73.321.200,00 €	- 2.200.000,00 €	- €	- 75.521.200,00 €	- €	- 57.027.600,00 €	- 800.000,00 €	- €	- 57.827.600,00 €	- 59.685.501,36 €	- 45.701.992,27 €
2042	7	0,759917813	- €	- 73.321.200,00 €	- 2.200.000,00 €	- €	- 75.521.200,00 €	- €	- 57.027.600,00 €	- 800.000,00 €	- €	- 57.827.600,00 €	- 57.389.905,15 €	- 43.944.223,33 €
2043	8	0,730690205	- €	- 73.321.200,00 €	- 2.200.000,00 €	- 10.220.000,00 €	- 85.741.200,00 €	- €	- 57.027.600,00 €	- 800.000,00 €	- 13.328.000,00 €	- 71.155.600,00 €	- 62.650.255,01 €	- 51.992.699,95 €
2044	9	0,702586736	- €	- 73.321.200,00 €	- 2.200.000,00 €	- €	- 75.521.200,00 €	- €	- 57.027.600,00 €	- 800.000,00 €	- €	- 57.827.600,00 €	- 53.060.193,37 €	- 40.628.904,71 €
2045	10	0,675564169	- €	- 73.321.200,00 €	- 2.200.000,00 €	- €	- 75.521.200,00 €	- €	- 57.027.600,00 €	- 800.000,00 €	- €	- 57.827.600,00 €	- 51.019.416,71 €	- 39.066.254,53 €
2046	11	0,649580932	- €	- 73.321.200,00 €	- 2.200.000,00 €	- €	- 75.521.200,00 €	- €	- 57.027.600,00 €	- 800.000,00 €	- €	- 57.827.600,00 €	- 49.057.131,45 €	- 37.563.706,28 €
2047	12	0,62459705	- €	- 73.321.200,00 €	- 2.200.000,00 €	- €	- 75.521.200,00 €	- €	- 57.027.600,00 €	- 800.000,00 €	- €	- 57.827.600,00 €	- 47.170.318,70 €	- 36.118.948,34 €
2048	13	0,600574086	- €	- 73.321.200,00 €	- 2.200.000,00 €	- €	- 75.521.200,00 €	- €	- 57.027.600,00 €	- 800.000,00 €	- €	- 57.827.600,00 €	- 45.356.075,67 €	- 34.729.758,02 €
2049	14	0,577475083	- €	- 73.321.200,00 €	- 2.200.000,00 €	- €	- 75.521.200,00 €	- €	- 57.027.600,00 €	- 800.000,00 €	- €	- 57.827.600,00 €	- 43.611.611,22 €	- 33.393.998,10 €
2050	15	0,555264503	- €	- 73.321.200,00 €	- 2.200.000,00 €	- €	- 75.521.200,00 €	- €	- 57.027.600,00 €	- 800.000,00 €	- €	- 57.827.600,00 €	- 41.934.241,56 €	- 32.109.613,56 €
2051	16	0,533908176	- €	- 73.321.200,00 €	- 2.200.000,00 €	- 10.220.000,00 €	- 85.741.200,00 €	- €	- 57.027.600,00 €	- 800.000,00 €	- 13.328.000,00 €	- 71.155.600,00 €	- 45.777.927,67 €	- 37.990.556,59 €
2052	17	0,513373246	- €	- 73.321.200,00 €	- 2.200.000,00 €	- €	- 75.521.200,00 €	- €	- 57.027.600,00 €	- 800.000,00 €	- €	- 57.827.600,00 €	- 38.770.563,57 €	- 29.687.142,71 €
2053	18	0,493628121	- €	- 73.321.200,00 €	- 2.200.000,00 €	- €	- 75.521.200,00 €	- €	- 57.027.600,00 €	- 800.000,00 €	- €	- 57.827.600,00 €	- 37.279.388,05 €	- 28.545.329,53 €
2054	19	0,474642424	- €	- 73.321.200,00 €	- 2.200.000,00 €	- €	- 75.521.200,00 €	- €	- 57.027.600,00 €	- 800.000,00 €	- €	- 57.827.600,00 €	- 35.845.565,44 €	- 27.447.432,24 €
2055	20	0,456386946	- €	- 73.321.200,00 €	- 2.200.000,00 €	- €	- 75.521.200,00 €	- €	- 57.027.600,00 €	- 800.000,00 €	- €	- 57.827.600,00 €	- 34.466.889,84 €	- 26.391.761,77 €
2056	21	0,438833602	- €	- 73.321.200,00 €	- 2.200.000,00 €	- €	- 75.521.200,00 €	- €	- 57.027.600,00 €	- 800.000,00 €	- €	- 57.827.600,00 €	- 33.141.240,23 €	- 25.376.694,01 €
2057	22	0,421955387	- €	- 73.321.200,00 €	- 2.200.000,00 €	- €	- 75.521.200,00 €	- €	- 57.027.600,00 €	- 800.000,00 €	- €	- 57.827.600,00 €	- 31.866.577,15 €	- 24.400.667,32 €
2058	23	0,405726333	- €	- 73.321.200,00 €	- 2.200.000,00 €	- €	- 75.521.200,00 €	- €	- 57.027.600,00 €	- 800.000,00 €	- €	- 57.827.600,00 €	- 30.640.939,56 €	- 23.462.180,11 €
												NPV	- 1.204.930.706,36 €	- 973.990.064,40 €
												NPC	1.204.930.706,36 €	973.990.064,40 €

Figure 9-2: Net present cost calculations of AEL and PEMEL plants.

G. Annual Production of Hydrogen Based on the Electrolysis Plant's Installed Power

$$m_{H_2,annual} = \frac{P_{el} * CF * 8760\ h/a}{LHV_{H_2}} * \eta_{system} \tag{9-5}$$

H. Specific Cost of Hydrogen Liquification

$$c_{spec,liq} = c_{spec,I\&O} + e_{spec,liq} * c_{el,green} \tag{9-6}$$

I. Specific Cost of Hydrogen Transportation

$$c_{spec,trans} = \frac{c_{spec,TCO,H_2-powered\ \ truck} * d_{avg,both\ ways} + c_{driver}}{m_{H_2}} \tag{9-7}$$

J. OpenVSP

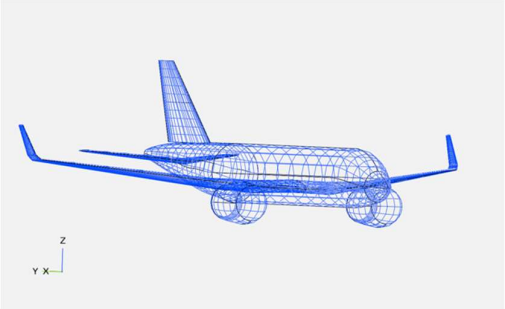

Figure 9-3: OpenVSP HyZero

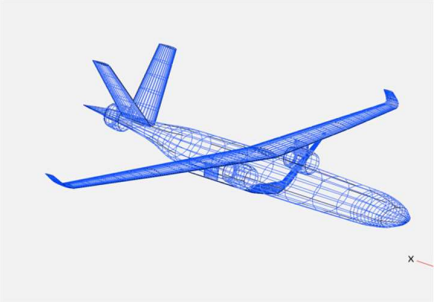

Figure 9-4: OpenVSP reference aircraft

K. Specific cost Calculation of Hydrogen Storage Infrastructure at the Airport

			Nominal cash flow				Discounted cash flow	
Year	Period	Discount Factor	Investment	Operation	Maintenance	Sum	Sum	
2035	0	1	-2.663.800,73 €			-2.663.800,73 €	- 2.663.800,73 €	
2036	1	0,961538462		-106.552,03 €		- 106.552,03 €	- 102.453,87 €	
2037	2	0,924556213		-106.552,03 €		- 106.552,03 €	- 98.513,34 €	
2038	3	0,888996359		-106.552,03 €		- 106.552,03 €	- 94.724,37 €	
2039	4	0,854804191		-106.552,03 €		- 106.552,03 €	- 91.081,12 €	
2040	5	0,821927107		-106.552,03 €		- 106.552,03 €	- 87.578,00 €	
2041	6	0,790314526		-106.552,03 €		- 106.552,03 €	- 84.209,62 €	
2042	7	0,759917813		-106.552,03 €		- 106.552,03 €	- 80.970,79 €	
2043	8	0,730690205		-106.552,03 €		- 106.552,03 €	- 77.856,52 €	
2044	9	0,702586736		-106.552,03 €		- 106.552,03 €	- 74.862,04 €	
2045	10	0,675564169		-106.552,03 €		- 106.552,03 €	- 71.982,73 €	
2046	11	0,649580932		-106.552,03 €		- 106.552,03 €	- 69.214,17 €	
2047	12	0,62459705		-106.552,03 €		- 106.552,03 €	- 66.552,08 €	
2048	13	0,600574086		-106.552,03 €		- 106.552,03 €	- 63.992,39 €	
2049	14	0,577475083		-106.552,03 €		- 106.552,03 €	- 61.531,14 €	
2050	15	0,555264503		-106.552,03 €		- 106.552,03 €	- 59.164,56 €	
2051	16	0,533908176		-106.552,03 €		- 106.552,03 €	- 56.889,00 €	
2052	17	0,513373246		-106.552,03 €		- 106.552,03 €	- 54.700,96 €	
2053	18	0,493628121		-106.552,03 €		- 106.552,03 €	- 52.597,08 €	
2054	19	0,474642424		-106.552,03 €		- 106.552,03 €	- 50.574,11 €	
2055	20	0,456386946		-106.552,03 €		- 106.552,03 €	- 48.628,96 €	
						-4.794.841,32 €	- 4.111.877,58 €	NPV
							4.111.877,58 €	NPC
							0,07358175	CRF
							302.559,15 €	annualized cost
							0,08 €	cost per kg_H2

Figure 9-5: Specific cost calculation of hydrogen storage infrastructure at the airport.

L. DOC Cost Structure

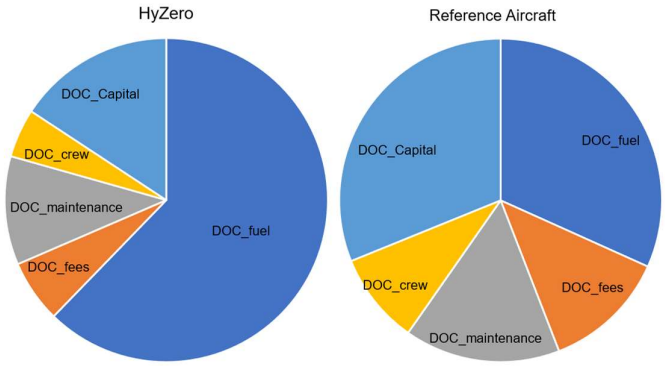

Figure 9-6: DOC Structure

M. Tank calculation

Assumptions

- Geometrical calculation as one tank
- Elliptical cone with ellipsoid domes on each side
- Pressure vessel formular for wall thickness calculation
- Constant wall thickness
- Wall made of Carbon fibre composite
- Mass factor for not calculated structure: 10 %
- Liner does not absorb tension, liner only holds H_2, liner covers all inner walls

Description	Equation & Value
Density liquid hydrogen	$\rho_{H_2} = 71\ kg/m^3$
Density aluminium	$\rho_{Al} = 2699\ kg/m^3$
Density foam	$\rho_{foam} = 32\ kg/m^3$
Density carbon fibre composite	$\rho_{carbon} = 1578\ kg/m^3$
Tensile strength	$\sigma = 546\ MPa$
Inner vessel pressure	$p = 1{,}45\ bar$
Safety	$S = 4$
Total wall thickness	$t = 16{,}1\ cm$
Liner thickness	$s_{liner} = 0{,}1\ mm$
Forward height	$H = 2{,}57\ m$
Aft height	$h = 1{,}51\ m$
Forward width	$B = 4{,}33\ m$
Aft width	$b = 2{,}16\ m$
Width to length ratio domes	$\frac{B}{l_{fwd}} = \frac{b}{l_{aft}} = 1{,}6$
Tank length without domes	$l = 3{,}382\ m$
Tank length with domes	$L = l + l_{fwd} + l_{aft} = 5{,}41\ m$
Volume forward dome	$V_{fwd} = \frac{\pi}{6} * B * H * l_{fwd} = 7{,}89\ m^3$
Volume aft dome	$V_{aft} = \frac{\pi}{6} * b * h * l_{aft} = 1{,}15\ m^3$
Volume cone	$V_{cone} = \frac{\pi}{12} * l * (H * B + \sqrt{H * B * h * b}\ + h * b) = 18{,}06\ m^3$
Total volume	$V = V_{cone} + V_{fwd} + V_{aft} = 27{,}10\ m^3$
Surface forward dome	$O_{fwd} = 15{,}83\ m^2$
Surface aft dome	$O_{aft} = 8{,}69\ m^2$
Surface cone	$O_{cone} = 28{,}81\ m^2$
Total outer surface	$O_i = O_{fwd} + O_{aft} + O_{cone} = 53{,}33\ m^2$
Surface inner wall	$O_{wall} = 15{,}92\ m^2$

pressure wall thickness	$s_i = S * \frac{p * D_{max}}{2 * \sigma} = S * \frac{p * B * 1{,}6}{2 * \sigma} = 3{,}68\ mm$
Inner wall thickness	$s_{wall} = S * \frac{p * L * 2}{2 * \sigma} = 5{,}75\ mm$
Pressure wall mass	$m_i = O_i * s_i * \rho_{carbon} = 310\ kg$
Inner wall mass	$m_{wall} = O_{wall} * s_{wall} * \rho_{carbon} = 144\ kg$
Liner mass	$m_{liner} = (O_i + 2 * O_{wall}) * s_{liner} * \rho_{Al} = 115\ kg$
Insulation mass	$m_{insul} = O_i * t * \rho_{foam} = 275\ kg$
Outer wall mass	$m_o = (O_{fwd} + O_{aft}) * s_i * \rho_{carbon} = 71\ kg$
Walls against slosh	$m_{anti-slosh} = 22\ kg$
Mass factor	$f = 1{,}25$
Total tank mass	$m = (m_i + m_{wall} + m_{liner} + m_{insul} + m_o + m_{anti-slosh}) * f = 1090\ kg$

N. BLI system and fuel cell mass estimation

Component	Mass [kg]	Source
Motor	60	Jansen.2019
Inverter	30	Jansen.2019
Nacelle	100	Lolis.2014
Bare engine (BLI)	290	Welstead.2016, Seitz.2021
Thermal management	30	Welstead.2016
Circuit Protection	30	Welstead.2016
Fuselage integration	150	Seitz.2021
Cable	50	Welstead.2016, Jansen.2019
FC	100	Kadyk.2018, HYZON Motors
Batteries	30	[Kadyk.2019]